NASA CONTRACTOR REPORT

NASA CR-1392

SUBSONIC SPHERE DRAG MEASUREMENTS AT INTERMEDIATE REYNOLDS NUMBERS

by Kenneth R. Sivier and J. A. Nicholls

Prepared by
UNIVERSITY OF MICHIGAN
Ann Arbor, Mich.
for Lewis Research Center

NATIONAL AERONAUTICS AND SPACE ADMINISTRATION • WASHINGTON, D. C. • JULY 1969

SUBSONIC SPHERE DRAG MEASUREMENTS AT INTERMEDIATE REYNOLDS NUMBERS

By Kenneth R. Sivier and J. A. Nicholls

Prepared under Grant No. NGR 23-005-003 by
UNIVERSITY OF MICHIGAN
Department of Aerospace Engineering
Ann Arbor, Mich.

for Lewis Research Center

NATIONAL AERONAUTICS AND SPACE ADMINISTRATION

For sale by the Clearinghouse for Federal Scientific and Technical Information
Springfield, Virginia 22151 – CFSTI price $3.00

ABSTRACT

The drag of spheres, at subsonic Mach numbers and Reynolds numbers from 25 to 4000, was studied in a continuous wind tunnel using a one-component, magnetic support-and-balance system. The low turbulence incompressible results verified this experimental approach, especially at Reynolds numbers below 300 where the spherical models were not disturbed by unsteady lateral forces. Measurements were also made to evaluate the effects of compressibility, slip flow (Knudsen numbers up to 0.04), sphere surface roughness, and free-stream turbulence (intensities up to 8%).

FOREWORD

The research described herein, which was conducted at the Gas Dynamics Laboratories, Department of Aerospace Engineering, University of Michigan, was performed under NASA Grant NGR 23-005-003 with Mr. H. Bankaitis, Chemical Rocket Division, NASA Lewis Research Center, as Project Manager.

TABLE OF CONTENTS

LIST OF ILLUSTRATIONS

SUMMARY

As part of an investigation of the dynamics of particulate combustion products occurring in rocket motor exhausts, an experimental study has been made of the drag of smooth and rough spheres at subsonic Mach numbers, Reynolds numbers (Re) from 25 to 4000, and free-stream turbulence intensities up to 8%. This study was carried out in a small, continuous, subsonic wind tunnel using a one-component, magnetic support-and-balance system to hold the spherical models in the test section and to measure the drag forces acting on them. This experimental approach was found to be well suited to the study of sphere drag, especially at Reynolds numbers below 300 where the sphere is not disturbed by unsteady lateral forces.

The low Mach number ($M \leq 0.23$), low turbulence, smooth sphere data were found to be in general agreement with the standard sphere drag data: the shape of the drag coefficient (C_D) vs. Re curve was verified, but values of C_D ranged from 8% ($Re \simeq 100$) to 20% ($Re \simeq 4000$) above the standard values. Higher turbulence levels (up to 8%) were found to produce a substantial increase in C_D at the higher values of Re; the C_D increase approached zero for $Re < 200$.

Some drag data were obtained at Knudsen numbers as high as 0.04. These data suggest a drag decrease due to slip effects, but the results are not conclusive. For $Re > 1000$, the usual continuum increase in C_D due to compressibility was observed.

Using the average outside diameter of a very rough sphere as the reference dimension, it was found that large scale surface roughness (ratio of roughness element size to sphere diameter in the range from 0.10 to 0.18) caused a small reduction in sphere drag for $Re < 500$ relative to the smooth sphere results. For $Re > 500$, large roughness was found to result in a systematic increase in C_D; the increase apparently correlating with ratio of the roughness element size to the boundary layer thickness.

The lateral motions, of the axially restrained spheres, were observed to correlate with the usual description of development of the separated region and wake in the laminar flow around a sphere. No significant changes in the lateral motion characteristics were observed due to roughening the spheres. However, the higher turbulence levels resulted in an earlier beginning (in terms of Reynolds number) of the shedding of the trailing ring vortex.

NOMENCLATURE

C_D	drag force coefficient
d	diameter, ft or in.
d_{act}	actual diameter of rough spheres, ft or in.
d_o	core sphere diameter, ft or in.
g	acceleration due to gravity
k	surface roughness factor; ratio of roughness element height to sphere diameter
Kn	Knudsen number; ratio of mean free path length to characteristic body dimension
M	Mach number; ratio of flow velocity to speed of sound
$\overline{M}$	mean value of M
ΔM	deviation from $\overline{M}$
n	load factor; total load divided by the body weight
p_o	settling chamber pressure, psi, psf, mm Hg
p_1	test section static pressure, psi, psf, mm Hg
Δp_1	$p_o - p_1$, psi, psf, mm Hg
q	dynamic pressure, psi, psf
Re	Reynolds number based on diameter, $\rho Ud/\mu$
Re_{cl}	lower critical Re
Re_{cu}	upper critical Re
S_{ref}	reference area, $in.^2$, ft^2
U	flow velocity, fps
$\overline{U}$	mean flow velocity, fps
ΔU	deviation from the mean flow velocity, fps
U_o	test section centerline flow velocity, fps
W	model weight, lb(m)

x'_{tv}	axial distance of the downstream throttling valve from its closed position, in.
Δx	recorder deflection, in.

γ	ratio of specific heats, 1. 4 for air
δ	boundary layer thickness, in.
μ	air viscosity, lb(m)/ft-sec
ρ	air density, lb(m)/ft^3

Subscripts and Superscripts

$\overline{(\ )}$	mean value
$(\ )_o$	total or settling chamber value: or centerline value
$(\ )_{rms}$	root-mean-square value

1. INTRODUCTION

The advent of metalized rocket fuels brought with it a new problem in two-phase flow. Metallic fuels are attractive because of their high heat of combustion. Calculations[1] have shown that metallic additives can increase the maximum specific impulse of a propellant by as much as 10 to 15%. However, this potential performance increase cannot be achieved fully. The metallic oxides and fluorides, formed in the combustion process, begin condensation in the combustion chamber. This condensation (together with particle agglomeration) continues in the nozzle expansion process. The resulting particulate material, that is being carried out of the nozzle by the gaseous combustion products, represents up to 50% of the total weight flow.

These particles are subject to thermal and velocity lags with respect to the gaseous nozzle flow. Calculations[2, 3, 4] have shown that these losses can range from a fraction of 1% to values approaching 10%. Thus, the particulate portion of the combustion products can produce losses that not only are significant compared to the thrust gains obtained by adding metallic fuels but also are significant compared to the total nozzle thrust.

Analytical techniques[5-10] are available that give qualitatively accurate predictions of the thrust losses due to particulate material in rocket exhausts. However, the quantitative accuracy of these predictions depends on

the accuracy to which the drag and heat transfer* coefficients and the size of the particles are known.

The mechanisms of particle formation and growth are becoming known (e.g., Ref. 11 and 12). It is now possible to make reasonable a priori estimates of particle size distributions for specific rocket motors. Furthermore, direct measurements[12, 13, 14] have established that the mean particle diameters fall in the range from 1 to 5 microns. This range is sufficiently precise to provide a good guide for investigating particle drag coefficients in the flow regimes of interest.

Figure 1 presents the results, in terms of relative Mach and Reynolds numbers†, of two calculations of the gasdynamic trajectories of "typical" particles in "typical" rocket motors. These calculations show that the trajectories lie principally in flow regimes characterized by rarefied gas effects; i.e., slip, transition, and free molecule flows. Only at the very lowest Mach numbers (corresponding to velocities occurring only in the combustion chamber) is the particle in continuum flow. Specifically, the Reynolds number range of interest extends downward from a few

*The effect of thermal lag on thrust is relatively small and, hence, a rough estimate of the heat transfer coefficient is often sufficient[6].

†The relative Mach and Reynolds numbers of a particle are calculated on the basis of the relative velocity between the particle and the gaseous nozzle flow.

hundred to values well below 1 (into the Stoke's flow regime); incompressible Mach numbers (in the slip and transition flow regimes) represent especially interesting conditions for the rocket-nozzle, two-phase flow problem.

Thus, this problem requires particle drag data for both compressible and rarefied flows. In addition, the effects of free stream turbulence and particle surface roughness must be included. Even assuming that the particles can be approximated by spheres, the available standard sphere drag data (obtained for smooth spheres in non-turbulent, incompressible, continuum flow) is not applicable directly. Particle data for more realistic flow conditions are scarce, and for many conditions are unavailable.

Sphere drag, and its relationship to gas-particle flows, is examined in detail in Ref. 6 and 17 through 22. Reference 23 presents some additional material, including a discussion of the combined effects of compressible and rarefied flows, turbulence, and surface roughness. Reference 23 also discusses briefly the more important sphere drag measurements that have been made under "non-standard" conditions. This latter discussion emphasizes the difficulties involved in obtaining particle drag data and illustrates the need for carefully controlled experiments capable of evaluating the individual gasdynamic effects.

The objective of the present investigation was to design such a controllable experiment and to carry out suitable sphere drag measurements, particularly at subsonic Mach numbers and Reynolds numbers low enough to obtain significant rarefied flow effects. The initial results are reported below. Essentially these results were the design, construction, and calibration of a suitable test facility, verification of the experimental approach by measuring the "standard" sphere drag curve, and some preliminary data under "non-standard" test conditions.

2. EXPERIMENTAL APPARATUS

2.1 INTRODUCTION

The general requirements for the experimental technique for the present investigation were: (1) good control of the test conditions, resulting in reliable experimental data; (2) the ability to validate the technique by obtaining sphere drag data under "standard" flow conditions; and (3) sufficient flexibility to permit the evaluation of the effects of rarefied flow, compressibility, free-stream turbulence, and surface roughness. One experimental tool that satisfies the above requirements is the continuous wind tunnel. However, this approach has two serious limitations with respect to sphere drag measurements at low Reynolds numbers. Most obvious is the model support interference, which would be expected to be significant at values of Re where the wake is beginning to form. In addition, the very small drag forces would result in severe problems in the use of a conventional mechanical drag balance.

The use of a magnetic support-and-balance system solves the problems involved in the use of a conventional mechanical support-and-balance system. First, and obviously, the experiment is free of a physical model support. Second, the practical unit of magnetic support force is the weight of the model alone. Since the ratio of aerodynamic force to model weight increases with decreasing model size, one finds that the use of

small models (necessary to achieve small Re) results in high drag forces (in model weight units) and a very sensitive magnetic balance for measuring otherwise very tiny drag forces. Finally, the design and operation of magnetic balance systems are well understood and their application to wind tunnel testing is not uncommon.

A small wind tunnel, incorporating a magnetic support-and-balance system, was developed. This wind tunnel was built with a simple subsonic test section; the later addition of a test section for testing at low supersonic Mach numbers is feasible. The details of the design, construction, and performance of the magnetic balance system are presented in Ref. 24. A discussion of the design, operation, and calibration of the wind tunnel is presented below.

2.2 WIND TUNNEL SYSTEM: DESIGN AND OPERATION

The general requirements for the wind tunnel to be used in this research were: (1) operation at subsonic Mach numbers, M, from the incompressible to values approaching 1.0, (2) operation at sphere Reynolds numbers, Re, from about 1000 down to as low as possible, and (3) continuous operation into the existing laboratory vacuum system. Once the test conditions (i.e., M and Re) were chosen, the most important design parameter was the test section diameter. In the present case, the diameter was limited on the small side by the expected side wall boundary layer growth (leading both to

a reduced diameter of inviscid flow and to an axial gradient in test conditions) and by its relationship to the model size. A too small ratio of test section diameter to model diameter would have led to the necessity of undesirable side wall proximity corrections while, on the large side, the test section diameter was limited by the capacity of the vacuum system and by the power requirements of the magnetic system's coils.

The resulting wind tunnel design represented a practical compromise of the above constraints plus several other less important ones. This compromise resulted in a test-section inside diameter of 2 in. Suitable spherical models (lapped precision ball bearings) were commercially available in diameters from 0.025 in. upward; diameters from 1/16 to 1/4 in. were selected for this research. The performance of the wind tunnel, with this range of sphere diameters, is shown in Fig. 2. Magnetic support limits are shown for an assumed maximum force capacity of three times the model weight, i.e., $n = 3$. The vacuum system limit is based on the geometrical test section area and steady-state operation. It does not include the effect of the laboratory's 13,000 cubic foot vacuum tank capacity, permitting operation for short periods at mass flows exceeding the pumping capacity. In practice it was found possible to obtain good low Mach number drag measurements at settling chamber pressures below 5 mm Hg.

A sketch of the wind tunnel system is presented in Fig. 3 and a photograph in Fig. 4. These figures show the magnetic system's coils installed. The test section was made of 2 in. I.D. by 1/4 in. wall Plexiglas tubing. It contained three 3/4 in. diameter windows (optical flats) mounted almost flush with the inside tube surface on their axial diameters. Two of these windows were for the model position sensor (Ref. 24); the third was for viewing of the model by means of a low power microscope.

The side of the test section, which did not contain a window, was fitted with five static pressure orifices arranged axially with spacings of 1 in. The farthest upstream orifice was located in the plane of the window centers and hence measured the wall static pressure at the axial location of the model. The orifice openings were 0.100 in. in diameter. An entrance port was located 2 1/2 in. below the plane of the window centers. It was used for installing total head pressure and hot wire probes.

Referring to Fig. 3, during operation room air entered the tunnel inlet through the upstream throttling valve. This valve was used to control the supply pressure. The throttled air passed through the inlet pipe and into the diffuser-and-screen section. This section served to reduce the velocity and turbulence level of the incoming air. The air then passed through the settling and contraction section and into the straight test section.

The downstream throttling valve was located immediately below the test section and was used to control test section Mach number. Normally,

this valve was operated choked. Therefore, the ratio of the effective areas between the test section and the (variable) valve throat uniquely determined the test section Mach number. After passing through the downstream throttling valve, the air entered vacuum piping leading to the vacuum system.

Except for a few steel bolts and some stainless steel turbulence damping screens, the entire tunnel above its attachment to the vacuum piping was made of either aluminum or Plexiglas. This was done to prevent the tunnel structure from distorting the magnetic fields generated by the magnetic coil systems.

2.3 INSTRUMENTATION

Except for the magnetic balance, the tunnel was instrumented mainly for pressure measurement. A schematic sketch of the pressure instrumentation system is shown in Fig. 5. The solid lines show the system configuration used during drag measurements. The settling chamber pressure was measured by two Wallace and Tiernan, aneroid-type, absolute pressure gauges (Type FA-160). These gauges had ranges of 0 to 20 mm Hg and 0 to 100 mm Hg absolute and a nominal precision of 1/3% of full scale. These gauges were calibrated to a precision of $\pm$ 1/4% of full scale for the 0 to 20 mm Hg gauge and $\pm$ 1/5% of full scale for the 0 to 100 mm Hg gauge.

Because the difference between total and static pressure is very small (compared to the absolute pressure) at the Mach numbers of interest in

this research and because this difference varies roughly linearly with Mach number, all test section pressures were measured differentially with respect to the settling chamber pressure. These differentials were measured on a Meriam precision, slant-tube, micromanometer (Model A-750) filled with Dow Corning No. 200 (5 centistoke viscosity) silicone fluid. This fluid had a specific gravity of about 0.92 at 25°C; the variation in specific gravity with temperature was accounted for in reducing the differential pressure data. The micromanometer had a mechanical precision of better than 0.001 in. in column height. The actual maximum uncertainty in reading a given differential pressure was about $\pm$ 0.002 in. of fluid.

During tunnel calibration, four additional side wall static pressures and a test section total head pressure were measured. As shown by the dashed lines in Fig. 5, for these tests the static pressure shut-off valve was replaced by a multi-position switching valve to facilitate measurement of the several pressures on the micromanometer.

Test section free-stream turbulence measurements were made using a DISA miniature hot-wire probe (Type 55A25). This probe incorporated a platinum plated tungsten wire approximately 0.040 in. long and 0.0002 in. in diameter. The probe had a nominal cold resistance of about 3.5 ohms. It was operated in the constant temperature mode using a Miller Model M-5 hot-wire amplifier unit, modified for wire resistances in the range

from 4 to 10 ohms. The DC voltage output of the amplifier unit was read on a Tektronix Type 565 dual-beam oscilloscope using a Type 2A63 differential amplifier plug-in module which had a maximum sensitivity of 1 millivolt per centimeter. The root-mean-square value of the voltage fluctuations (from the mean DC voltage value) of the amplifier unit output was measured by a Ballantine Laboratories Model No. 320 true root-mean-square voltmeter.

2.4 WIND TUNNEL CALIBRATION

Initially, a tunnel inlet was used that was mechanically simple but aerodynamically poor. The resulting test section turbulence levels were unacceptably high, requiring the installation of a new inlet section (shown in Fig. 3 and 4). Sketches of the internal configurations of the two inlets are compared in Fig. 6. Most calibration results presented below are for the modified inlet only. However, the Mach number and velocity distribution results apply qualitatively to the original inlet as well; turbulence data are presented for both inlets.

Test section centerline Mach numbers, as a function of p_o, are presented in Fig. 7 for several values of x_{tv}', the axial distance of the downstream throttling valve from its closed position ($x_{tv}' = 0$ for $M = 0$). Generally, the data fall within $\pm .005$ M of the mean curve and show only a small influence of pressure level. The magnitude of the axial centerline

Mach number gradient is indicated in Fig. 8. The axial Mach number increase was due to the growth of the wall boundary layer and became significant only at the higher M's.

Transverse velocity distribution data were obtained from a series of total head pressure surveys across the test section in the plane of the window centers. The probe was made of 1/8 in. outside diameter tubing; the end was square and beveled internally. Since the probe was used only to determine the flow uniformity and the location of the outer edge of the boundary layer, no attempt was made to correct the data for possible viscous and slip effects. However, the stagnation pressure (outside of the boundary layer) measured by the probe was found to be, on the average, extremely close to the stilling chamber stagnation pressure. The probe diameter was too large to obtain meaningful data close to the wall, but it did permit the determination of the outer edge of the boundary layer for boundary layer thicknesses greater than about 0.1 in.

Some results of the total head probe surveys are presented in Fig. 9. The total head data have been converted to velocity distributions, non-dimensionalized by the centerline velocity, U_o. The results are for those flow conditions which gave the thickest boundary layers. Although the free-stream data, for these low p_o, low M conditions, exhibited a fair amount of scatter about the unity velocity ratio, no systematic deviation was observed. In the main, the scatter seemed to be due to measured total

head pressure differentials being generally only about one order of magnitude, or less, greater than the reading accuracy of the manometer. The resulting random errors resulted in a detectable scatter in the velocity data. The scatter was found to be much less at larger values of p_o and M. On this basis, it was concluded that the free-stream flow was satisfactorily uniform.

The boundary layer thicknesses indicated in Fig. 9 are on the pessimistic side. The indicated radial distances were measured with respect to the centerline of the total head probe. However, the probe began to sense the edge of the boundary layer when the probe centerline was still about one probe radius (about 0.06 in.) from the edge. Thus the boundary layer thicknesses were about 0.06 in. less than indicated by Fig. 9. On this basis, the indicated boundary layer thicknesses, at 99% of the free-stream velocity, varied downwards from a maximum of about 0.4 in.

Since one objective of this research was the measurement of sphere drag in effectively turbulence free flow, the measurement of the test section turbulence levels was of special interest. The turbulence levels were evaluated from measurements made with a single hot wire, oriented at right angles to the free-stream flow and operated in the constant temperature mode at a single wire temperature. The root-mean-square turbulence intensities, in the form of the ratio $\Delta M_{rms}/\bar{M}$, determined from these

measurements, are presented in Fig. 10. Comparable data are shown for both the initial and modified inlet configurations. It is clear that the inlet modifications were effective in substantially reducing the level of turbulence. Unfortunately, the turbulence level was still significant, particularly at the higher pressures, and the resulting drag data cannot a priori be considered to be free of turbulence effects.

3. SPHERE DRAG MEASUREMENTS

3.1 EXPERIMENTAL TECHNIQUES

3.1.1 Models

Spherical models were used for all drag measurements made in this investigation. The spheres were classified according to their surface roughness, i.e., smooth, roughened (moderately rough), and very rough. The smooth models were commerical precision stainless steel ball bearings graded according to their surface finish. The two grades used were grade 5 (0.7 micro-inch rms surface finish) and grade 25 (1.5 micro-inch rms surface finish).

The roughened spheres were made by tumbling smooth spheres inside a cup-shaped grinding wheel. Figure 11 presents photographs of smooth and roughened spheres and Fig. 12 presents photomicrographs of the corresponding surfaces. Since no change in sphere weight (to within 10^{-4} grams) or diameter (to within 10^{-3} in.) could be detected after tumbling, it appeared that the tumbling punched and gouged small craters in the sphere's surface, rather than cutting and removing material. Based on inspection of the photomicrographs, the surface roughness element sizes (assuming that the crater depth is approximately equal to the crater diameter) were estimated to be as follows.

	Roughness Element Size (in.)
Initial Tumbling Effort	0.003
No. 100 Grit Wheel	0.002
No. 60 Grit Wheel	0.003

The very rough spheres were made by cementing roughening elements to roughened spheres. Of the many rough spheres made, only the most spherical and those with the most uniform coating were selected for testing. Figure 13 presents photographs of the three grades of very rough spheres. The roughening elements were 200μ (0.008 in. diameter) glass beads, 390μ (0.015 in.) glass beads, and a coarse abrasive having grit dimensions in the range from 0.015 to 0.025 in. with an apparent average of about 0.020 in. The rough spheres were weighed on a precision balance; their outside diameters were determined by taking the average of from four to six measurements (for each sphere) made with a toolmaker's microscope.

3.1.2 Testing Procedure

The model was inserted with the tunnel inlet assembly removed and the magnetic support system operating. The model was held by a magnetic insertion probe (Fig. 14) that was inserted into the test section from the upstream end and was held in a jig to permit precision positioning. The magnetic field of the support system magnetized the steel rod

sufficiently to hold the model tightly against the non-magnetic tip; the rod was positioned so that it did not touch the model. The probe was lowered until the model just touched the support system's light beam, used for sensing the model position. The model was released by withdrawing the steel rod from the probe; the slowly falling model was easily caught and held by the magnetic support system.

The levitated model was observed to have a small vertical oscillation. This was traced to a 60 cps ripple in the DC power supply used with the support system's control system. The resulting 60 cps oscillation of the model had an amplitude of from 0.010 to 0.015 in. for all sphere diameters and wind tunnel flow conditions.

Once the model was levitated, the tunnel inlet was replaced and the tunnel was evacuated by opening a downstream valve to the vacuum system. Under this evacuated, no-flow condition, the balance system was calibrated by noting the balance system's output (the deflection of a pen-type recorder). This output corresponded to the one g, or n = 1, loading condition.

During the sphere drag tests, corresponding values of p_o, Δp_1, and recorder deflection Δx were recorded. These, together with room temperature, comprised all of the data taken during a test.

Finally, the model insertion procedure could be reversed to retrieve a model after a test. This procedure was particularly valuable for the very rough spheres, where it was desired to run more than one test on a given model.

3.1.3 Data Reduction

The flow Mach number was determined from the pressure readings, p_o and Δp_1, through the isentropic flow relationship, i.e.,

$$M = f(\Delta p_1/p_o)$$

The corresponding dynamic pressure was found directly from the expression

$$q = \frac{1}{2}\gamma p_1 M^2$$

where

$$p_1 = p_o - \Delta p_1$$

M and q data from a typical drag test are presented in Fig. 15(a). The M drop-off below about 5 mm Hg was due to unchoking of the downstream throttling valve at low values of p_o. In this particular test, a large number of data points were taken at small values of p_o because of the interest in sphere drag at low values of Re. The gap in the data between p_o's of 18 and 38 mm Hg will be discussed below.

The recorder deflection data were converted to drag force data by comparing with the calibration (n = 1) deflection, i.e.,

$$\text{Dimensionless Drag Force} = n - 1$$

$$= \frac{(\Delta x)_{total} - (\Delta x)_{n=1}}{(\Delta x)_{n=1}}$$

Figure 15(b) presents the drag force data corresponding to the M and q data shown in Fig. 15(a). The high quality of magnetic balance data is clearly evident. These data, as well as all other drag data, were not corrected for a slightly non-linear balance response. This correction was neglected because (1) most drag loads were equal to or less than one g where the correction was small compared to the scatter in the data and (2) comparison of drag coefficients obtained using different sphere diameters (at the same M, Re condition) indicated no systematic variation attributable to the non-linear balance response.

The drag coefficient was calculated from the expression

$$C_D = \frac{\text{Drag Force}}{q\, S_{ref}}$$

which for this experiment could be written as

$$C_D = \frac{4W}{\pi d^2} \frac{n - 1}{q}$$

where W was the model weight and $4W/\pi d^2$ was a constant for each model used. Values of $(n - 1)/q$ are also presented in Fig. 15(b). These data illustrate the quality of drag coefficient data obtained in this investigation.

3.2 DISCUSSION OF SPHERE DRAG DATA

3.2.1 Smooth Spheres

Smooth sphere drag coefficient data are presented in Fig. 16 and 17 for Mach numbers of 0.16 and 0.23, respectively. These data were obtained with model diameters of 1/16, 1/8, and 1/4 in. The generally excellent agreement between the results for the different model diameters and between the results for the two incompressible M's (both situations implying different p_o's, turbulence levels, and balance loads for equal values of Re) argues for the general validity of the experimental technique and results.

The substantially greater spread in the low Re data for M = 0.16 (Fig. 16) is unexplained. Each symbol type for the 1/16 in. model refers to a separate test; the three tests were spread over a period of one month. Each data set by itself appears good and is self-consistent, even though operational and instrumentation problems are increasing at the low Re, low M test conditions. The 1/16 in. model data for M = 0.23 (Fig. 17) also represent three separate tests; in this case the data cluster around a mean curve with a maximum scatter of about $\pm$ 4%.

The standard drag curve, included in Fig. 16 and 17, is based on data found in Ref. 25, 26, and 27. A comparison of this standard curve with the results of the present experiments shows a systematic upward

shift of the data. For example, the M = 0.23 data has shifted upward by about 8% at Re = 100 and by about 20% at Re = 4000. The two known discrepancies in the present experiments, compared to the "standard" test conditions, were (1) the small vertical oscillation of the model and (2) the presence of a low level (.3 to 1.5%) test section turbulence intensity. The effect of the small (maximum velocity on the order of 0.2 fps) vertical oscillation is not known. The smooth sphere data, compared at equal values of Re but various combinations of M and sphere diameter, show no systematic variation due to turbulence. However, the range of turbulence intensity involved in such comparisons was small and, hence, the possibility remains that the C_D shift was due to low level free-stream turbulence.

An inspection of Fig. 16 and 17 reveals no data for the 1/16 in. or 1/8 in. spheres and very little data for the 1/4 in. spheres for Re from about 300 to 550. This is typical of all the smooth sphere data and was due to excessive radial motion of the models. In many cases, this motion was so large that the model moved outside the control system's light beam and was dropped. Typically, the model was stable and almost motionless (laterally) at Re $<$ 200. In the Re range from about 200 to 250, a very small, low frequency (several seconds per cycle) irregular lateral oscillation began. This motion slowly increased, both in extent and frequency, as Re was increased. At some critical Re, near 300, the extent of the lateral motion increased abruptly, quickly growing to a size where retention

of the model was marginal or impossible. If, however, Re was quickly increased (by increasing p_o) to a value exceeding 600, the lateral motions, while substantial, no longer exceeded the light beam width and drag data could be taken. It is well to emphasize that all data for Re $<$ 300 corresponds to motionless, or nearly so, models and for Re $>$ 300 the models had a substantial lateral motion.

The source of the observed lateral motion of the spheres is believed to be related to the development of the separated region, on the rearward face, and the wake. Excellent descriptions of the local sphere flow field are presented in Ref. 6 and 18. In brief, no flow separation is evident at low Re. Flow separation first appears (Ref. 28 and 29) at a value of Re slightly greater than 20. This separated region grows with Re, and the downstream end, enclosing the attached ring vortex, begins oscillation at Re $\simeq$ 100. This oscillation increases with Re until at Re $\simeq$ 300 the separation points begin to oscillate. The oscillation continues to increase until, at Re $\simeq$ 500, a periodic (but non-axisymmetric) shedding of ring vortices begins. The value of Re at which vortex shedding begins is often referred to as the lower critical Reynolds number, Re_{cl}. It signifies the appearance of a wake in which the flow around the sphere is no longer closed. The vortex shedding frequency increases rapidly with Re; based on existing shedding frequency data (summarized in Ref. 18), at Re = 1000 and M $\simeq$ 0.2 the frequency of shedding from a 1/8 in. sphere should be of the order of 5000 cps.

The magnetically supported models were restrained radially by a weak magnetic spring. The measured natural lateral frequency of the models (without drag loading and independent of model diameter) was about 2.3 cps. This frequency should increase as the square root of the total load on the model. Thus, even with the largest drag loads (n = 3) experienced in this experiment, the natural lateral frequency should not have exceeded 4 cps.

On the basis of the above discussions, it appeared that the observed lateral model motions were a result of the model/magnetic spring response to lateral aerodynamic loads caused first by the oscillation of the separated flow region and then by the non-axisymmetric shedding of the trailing ring vortex. Initially the lateral loads were low and the oscillation was of very low frequency. However, at Re $\simeq$ 300 the motion of the separation points produced substantial lateral forces oscillating at a frequency of several cps. For Re $>$ 500, the frequency of the lateral forces become high enough so that the model response was substantially reduced. This description is obviously oversimplified. For example, the model response should be negligible to the kilocycle level force oscillation expected at Re $\geq$ 1000. The lateral force oscillations are likely far more complex than the simple single frequency described above. However, this description of the source of the lateral motions seems qualitatively reasonable.

Data showing the effect of Mach number on sphere drag is presented in Fig. 18. These data were obtained by cross-plotting curves of C_D vs. Re.

At the low values of Re, the flow conditions penetrate deeply into the slip flow regime ($10^{-1} > Kn > 10^{-2}$). No drag rise due to compressibility is evident and, at least at Re = 150, a beginning indication of a drag decrease with increasing slip is found. Reference 30 suggests that the decrease in friction drag due to slip should be of the same order as Kn. Furthermore, the calculations of Ref. 28 show that skin friction accounts for roughly one-half of the sphere drag at values of Re in the neighborhood of 100. Thus, the Re = 150 data of Fig. 18 show a drag drop roughly agreeing with these estimates; a drag decrease of about 4% at $Kn = 4.2 \times 10^{-2}$. Unfortunately, higher values of Kn were precluded by the operational limitations of the wind tunnel facility and the results shown in Fig. 18 can serve only as a suggestion of the rarefied flow effects.

Under continuum flow conditions, the Re = 4000 data shown in Fig. 18 demonstrate, in another way, the overall validity of the experimental technique. The effect of compressibility at this value of Re was well demonstrated.

3.2.2 Rough Spheres

A major objective of the research, after verification of the experimental technique, was to investigate the effects of roughness on sphere drag. The initial measurements were made with roughened spheres. Typical results are shown in Fig. 19. The deviation of these data from

the experimentally determined smooth sphere results is negligible. Both spheres used in these tests had a roughness factor k of about 0.024. At Re = 1000, the ratio of stagnation point bounday layer thickness to sphere diameter is about 0.045. Thus, the roughness elements of these spheres were substantially smaller than the boundary layer, even at the largest Re for which data are presented.

It should be noted that data were obtained in the Re range from 300 to 600. Although the lateral motion characteristics were qualitatively similar to the smooth spheres, the size of the lateral motions was sufficiently less so as to permit satisfactory testing.

The lack of influence of roughening on sphere drag led to the use of very rough spheres in an effort to establish the degree of roughness required to influence, substantially, sphere drag. The results of these measurements are shown in Fig. 20 and 21. In reducing these data, it was necessary to use some reasonable, characteristic diameter of the rough spheres. The results presented in Fig. 20 and 21 are based on the actual average outside diameter of the rough spheres, the most unambiguous of the possible diameter selections. In these figures, d_o denotes the diameter of the core sphere (the sphere to which the roughening elements were cemented). The geometric characteristics of the spheres are tabulated below.

Geometry of Very Rough Spheres

d_o, in.	Roughness Element	$d_{act.}$, in.	k
1/16	200μ Spheres	0.081	0.099
1/16	390μ Spheres	0.091	0.175
1/8	Coarse Grit	0.159	0.126
3/16	Coarse Grit	0.226	0.088
1/4	200μ Spheres	0.272	0.029
1/4	390μ Spheres	0.286	0.056
1/4	Coarse Grit	0.287	0.070

Here k was calculated as the ratio of the characteristic dimension of the roughness element to the actual diameter of the sphere.

Figures 20 and 21 show two interesting characteristics of the effect of large roughness on sphere drag. First, with C_D calculated on the basis of outside sphere diameter, the overall effect of roughness is not great. Second, the effect of roughness is distinctly different above and below Re $\simeq$ 500. At low values of Re (at least down to Re $\simeq$ 40), C_D is reduced and no systematic effect of the different roughnesses is apparent. Curiously, the very rough sphere C_D's lie generally closer to the standard curve than do the smooth sphere C_D's. At the very low Re's (say Re $<$ 50), the effect of roughness appears to diminish. This is not surprising since at such low Re's, the viscous region around the sphere must be very large and even these rough spheres should be aerodynamically smooth.

It is quite possible that the decrease in C_D (compared to the smooth spheres) at Re $<$ 500 was not due to a corresponding drag decrease. It seems plausible that the large roughness elements of these spheres (k = 0.088 to 0.17) was producing a drag force increment that diminished with decreasing Re due to the rapidly thickening viscous region. To properly reduce these data, some effective sphere diameter (smaller than the outside diameter) should be used. This effective diameter should be a function of the shape of the roughness element and, more importantly, of the thickness of the boundary layer (or viscous region) or, rather, of Re. At very low values of Re, any reasonable, uniform roughness will be small compared to the viscous region, the rough sphere will be "aerodynamically" smooth, and the outside diameter of the sphere is correct for determining the reference area. At high values of Re where the roughness elements are large compared to the boundary layer thickness, the roughness elements will appear aerodynamically as projections above the sphere surface and some smaller diameter (even the core sphere diameter for an open pattern of roughness) should be used for data reduction. Such refinements in the determination of the "correct" effective sphere diameter require a far more detailed investigation than has been carried out here. In spite of this, as a practical matter, it appears that for Re $<$ 500 the use of the outside diameter and the standard values of C_D is sufficient.

Figure 21 shows that, above Re $\simeq$ 500 (Re_{cl} for smooth spheres), C_D increased due to roughness. Here the roughness effect was systematic, with C_D increasing both with increasing roughness and decreasing boundary layer thickness. The separation between the data possibly would be increased by the use of appropriate effective diameters. One would expect that, for equal outside diameters, the effective diameter for the craggy, abrasive-roughened sphere would be less than that for a sphere roughened by small spheres where the effective diameter should be about one roughening sphere radius outside the core sphere surface. The data for 1/4 in. spheres roughened with 200μ spheres and coarse grit abrasive have been replotted in Fig. 22 in terms of the ratio of rough to smooth sphere drag coefficient vs. the ratio of the roughness element size to the boundary layer thickness. These curves are based on the faired data of Fig. 21 for $1000 \leq Re \leq 3500$. Although the agreement between these data is not good, both curves exhibit qualitatively similar increases in drag with kd/δ. It is possible that agreement would be improved by the use of the correct effective diameters.

Two possible sources of the drag rise suggest themselves. First, as the roughness elements rise into the higher velocity part of the boundary layer and out into the surrounding flow, the effective wetted surface area of the sphere increases and it is likely that skin friction drag increases.

Second, as the roughness elements rise into the higher speed flow, they begin to shed eddies. While not able to cause transition of the boundary layer in the normal sense, these eddies will be present in the boundary flow to interact with the sphere wake, producing a decrease in base pressure and an increase in drag.

This last point raises the question of the significance of roughness effect crossover at Re = 500. On the basis of the above remarks about the correct effective diameter, the crossover appearing in Fig. 20 and 21 may be fortuitous and may not be related to a significant change in the character of the flow field. Such an off-hand dismissal is not completely satisfactory in view of the crossover of data from two different rough spheres shown in Fig. 21. If, even for the cases of very rough spheres, Re_{cl} occurs at Re $\simeq$ 500, then no trailing wake exists below this value of Re. If, in addition, the drag rise is primarily related to the wake flow, then the drag crossover at Re $\simeq$ 500 follows from a specific physical event. Unfortunately, the results obtained in this research are inadequate to do more than raise interesting questions on this subject.

While testing the very rough spheres, it was observed that these models were spinning at relatively high speed. Compared to the smooth spheres that exhibited rotational periods of several seconds per revolution, the rough spheres typically rotated around an axis parallel to the flow at speeds of from 10 to 30 rps. (These speeds were measured by

using a strobe light.) In a general way, the rotational speed started from zero at very low pressures, increased and then decreased as Re was increased, and appeared to decrease toward zero as Re exceeded 300. In one case, it was found that the sphere rotation reversed direction at $Re \simeq 300$ and continued to rotate at higher Re's. Typically, the rotation at low Re was clockwise (looking upstream), although in a few cases this was reversed. The source of this rotation is unknown although irregular roughness distributions or rotating phenomena in the separated flow region are possibilities. The peripheral velocity of these rotating spheres was low compared to the free stream velocity; e.g., for a 1/8 in. diameter model, rotating at 30 rps in a $M = 0.15$ flow, the ratio of peripheral velocity to free-stream velocity is approximately 0.006.

This type of sphere rotation is referred to as "screw motion." The effect of screw motion on sphere drag is reviewed in Ref. 20. Based on the results of the studies that have been made of this problem (none of which involve rough spheres), it appears that the affect of screw motion becomes significant only when the ratio of the peripheral velocity to the free-stream velocity is of the order of unity. On this basis, it was concluded that the low-speed screw motion that occurred in the present rough sphere studies did not influence the drag.

The results of these tests with very rough spheres support Selberg's conclusion (Ref. 32) that roughness can produce large drag increases at intermediate values of Re. The roughness elements on Selberg's spheres were not uniformly distributed; the largest appeared randomly and projected above the surface of the spheres. It appears reasonable to attribute part of Selberg's large data scatter to this random roughness. In reducing his data, Selberg used the core sphere diameter. This may, in part, explain his generally higher (compared to the present results) roughness induced C_D increase and the persistence of this increase down to Re $\simeq$ 200.

3.2.3 Free-Stream Turbulence

Before installing the modified wind tunnel inlet, some sphere drag data were obtained with the original inlet. As shown by Fig. 10, these data should reflect the influence of a substantial level of free-stream turbulence. Typical data from these early measurements, using smooth spheres, are presented in Fig. 23. Once again, the general agreement between data obtained with different model diameters (implying different p_o's and turbulence intensities for equal values of Re) indicates the validity of the experiment. A general and substantial increase in drag is caused by the turbulence. However, there is a strong suggestion that the effect of free-stream turbulence decreases with decreasing Re and, for the turbulence intensities involved here, is no longer significant for Re $<$ 200. (The turbulence intensity corresponding to the 1/16 in. diameter model data of Fig. 23 was about 4.5%.)

In Ref. 21 and 33, Torobin and Gauvin propose the parameter $(\Delta U_{rms}/\bar{U})^2$ Re as an indicator of the effect of free-stream turbulence on the flow adjacent to the sphere's surface. When this parameter reached a value of 45, they found that the boundary flow was sufficiently perturbed to trigger a sharp drag decrease characteristic of the boundary-layer transition at the upper critical Reynolds number, Re_{cu}*. The data of Fig. 23 have been replotted in Fig. 24 in the form of the ratio of the turbulent-flow C_D to the low-turbulence, smooth-sphere C_D vs. $(\Delta M_{rms}/\bar{M})^2$ Re. In spite of the data scatter (a maximum of about $\pm$ 8% for the data shown), the general increase of C_D with $(\Delta M_{rms}/\bar{M})^2$ Re is apparent. Projecting these data to the "transition" value, a maximum C_D increase of 20 to 35% is indicated. Qualitatively, this drag increase prior to "transition" is in agreement with the results of Torobin and Gauvin[33].

The characteristics of the lateral motions of the models were somewhat different in the presence of large free-stream turbulence. The difficult region between Re = 300 and Re = 550 did not exist. Large lateral motions occurred at values of Re below about 125 to 150. At higher Re's, the spheres were perturbed laterally much like the smooth spheres with

---

*In turbulence free, incompressible flow, Re_{cu} is slightly greater than 10^5 for spheres.

the modified inlet at Re $>$ 550. It appears that free-stream turbulence upsets the classical history of separated flow and wake development and causes vortex shedding to begin at much lower Re's.

The measured drag increase is probably due to interaction of the turbulence with the wake flow (of the type discussed in Ref. 34), causing a lowered base pressure and a correspondingly increased drag. At lower values of Re (Re $<$ 150) where the vortex shedding has not begun, this interaction is less effective and the drag increase is less. At very low Re, since one expects the turbulence to be unable to penetrate the thick, laminar viscous region around the sphere, no effect of turbulence should occur.

4. CONCLUSIONS

This research has been concerned with the experimental study of the drag of spherical particles under flow conditions corresponding to the solids-gas flows occurring in rocket nozzles. The specific objectives of the research were, first, the development of a suitable experimental technique and, second, the use of this technique to gain some insight into the general problem of sphere drag at intermediate Reynolds numbers; i.e., $10 \leq Re \leq 10,000$. An experimental technique was developed and found to be effective in the study of some important facets of the sphere drag problem. Some preliminary sphere drag data were obtained. The answers to a few questions were suggested, some welcome light was cast on several of the problems in subsonic sphere drag, and several new avenues of investigation were suggested. Most important of the results, however, is that the research has provided some experimental data under conditions of Mach number, Reynolds number, turbulence, and surface roughness for which previously no data existed.

The conclusions, resulting from this research, fall into two general categories: those related to the experimental technique and those concerned with the sphere drag measurements. The following observations and conclusions concern the experimental technique.

1. The application of the conventional wind tunnel, together with a magnetic support-and-balance system, to the measurement of sphere drag was successful. The absence of support interference and the high drag sensitivity (particularly at low Reynolds numbers) of the magnetic balance makes this technique especially useful for subsonic flow conditions at Re $<$ 10,000.

2. The experimental technique was verified by obtaining data very close to the "standard" sphere drag curve. The curve shape was reproduced and the small discrepancy in the C_D level is possibly due to two small defects remaining in the experiment; i.e., a small 60 cps vertical model jitter and a low level (0.3 to 1.5%) of turbulence. However, the excellent repeatability of the incompressible drag data under several different test conditions, indicates that the experimental results are reliable and that elimination of the defects of the experiment will serve only to verify the "standard" curve.

3. The one-component magnetic support is exceptionally well suited for studying the subsonic drag of spheres, in non-turbulent flow, at Reynolds numbers below about 300. Under such conditions, the lateral perturbations of the model are very small, or are absent, and natural radial stability is sufficient to hold the model laterally. The one-component support is less satisfactory

at Re $>$ 300 and in turbulent flows. Even here, reliable drag data can be obtained, although the model has a substantial lateral motion.

Aerodynamically, the results of the sphere drag research can be summarized by the following observations and conclusions.

4. The incompressible, low turbulence results with smooth spherical models are in essential agreement with the classical "standard" drag curve.
5. At the lower values of Re (less than about 200) no compressible drag rise was detected for M $\leq$ .51. However, at Re = 150 a drag decrease with increasing M was found. This decrease was of the correct magnitude for the skin friction drag decrease due to the effect of slip flow.
6. For Re $>$ 1000, the typical continuum, compressible flow drag rise was observed.
7. For Re $<$ 1000, sphere drag is not affected by a uniform distribution of concave (craters, gouges, etc.) roughness elements having dimensions equal to or less than one-half the boundary layer thickness. Spheres with roughness of this sort are aerodynamically smooth.

8. Uniform distributions of very large, projecting surface roughness elements (k = 0.09 to 0.18) cause a decrease in C_D at low Re, provided the average outside diameter of the rough sphere is used as the reference dimension. The decrease in C_D brings it in general agreement with the "standard" drag curve. The effect of roughness appears to tend to zero for $Re < 50$ and does go to zero at $Re \simeq 500$.

9. For $Re > 500$, large surface roughness elements (k = 0.03 to 0.07) produce a definite and systematic increase in C_D; C_D increasing both with increasing roughness and with increasing Re. Both of these affects apparently are due to an increase in roughness height compared to the boundary layer thickness.

10. Moderate free-stream turbulence intensities ($\leq 8\%$) produce a definite increase in C_D for $Re > 200$, the increase growing with increasing Re. There is evidence that for $Re < 200$, these turbulence levels produce little or no change in C_D, compared to the C_D's measured at lower turbulence intensities ($\simeq 1\%$). It appears, therefore, that for $Re < 200$ the difference between the present results and the standard sphere drag curve is not due to the low turbulence intensity remaining in the test section flow (conclusion no. 2 above).

11. The characteristics of the lateral motion of a smooth sphere in a low turbulence flow correspond generally to the accepted development history of the separated flow and wake. Apparently, the models respond first to the oscillating separated flow at the rear of the sphere and then, at Re $>$ 500, to the non-axisymmetric vortex shedding. The general characteristics of the lateral motion are not changed due to sphere roughness. However, high free-stream turbulence apparently shifts the beginning of vortex shedding to a much lower value of Re.

12. No evidence was found to support the findings of Ref. 35 and 36, showing variations of C_D with Re very different from that of the "standard" drag curve. The results of the present research show that the shape of the "standard" drag curve is essentially correct, even in the presence of large surface roughness and moderate levels of free-stream turbulence. (The turbulence levels encountered in this research were somewhat too low to achieve the steep drag drops reported in Ref. 33.)

13. The present results lend support to the findings of Ref. 32 and 37. Selberg's[32] high drag results could very well be due to roughness since the present results show substantial C_D increases at Re $\simeq$ 1000 for k $<$ 0.1. The increase in C_D, indicated by the present results,

would have been greater and would have persisted to lower values of Re if the sphere core diameter, instead of the outside diameter, had been used as the reference dimension.

Relative to the application of these results to the rocket nozzle problem, a decreasing influence of surface roughness and turbulence on C_D was observed for the lower Reynolds numbers, i.e., $Re < 200$. However this observation requires additional verification at very high turbulence intensities and for substantially more irregular particle shapes. In addition, it is clear that under the flow conditions occurring in the rocket nozzle, the particle drag will be influenced significantly by the combined effects of gas rarefaction and compressibility. The experimental investigation of these combined effects represents a major area in which additional research is required.

5. REFERENCES

1. Gordon, L.J. and Lee, J.B., "Metals as Fuels in Multicomponent Propellants," ARS J., Vol. 32, No. 4, April 1962, p. 600.

2. Bailey, W.S. et al, "Gas Particle Flow in an Axisymmetric Nozzle," ARS J., Vol. 31, No. 6, June 1961, p. 793.

3. Gilbert, M., Allport, J., and Dunlap, R., "Dynamics of Two-Phase Flow in Rocket Nozzles," ARS J., Vol. 32, No. 12, December 1962, p. 1929.

4. Marble, F.E., "Nozzle Contours for Minimum Particle-Lag Loss," AIAA J., Vol. 1, No. 12, December 1963, p. 2793.

5. Kliegel, J.R., "One Dimensional Flow of a Gas Particle System," Space Tech. Labs. TR-59-0000-00746, 1959.

6. Hoglund, R.F., "Recent Advances in Gas-Particle Nozzle Flows," ARS J., Vol. 32, No. 5, May 1962, p. 662.

7. Rannie, W.D., "A Perturbation Analysis of One-Dimensional Heterogeneous Flow in Rocket Nozzles," Progress in Astronautics and Rocketry: Detonation and Two-Phase Flow, Vol. 6, Academic Press, New York, 1962.

8. Marble, F.E., "Dynamics of a Gas Containing Small Solid Particles," Proceedings of the Fifth AGARD Combustion and Propulsion Colloquium, Pergamon Press, New York, 1963.

9. Hoffman, J.D. and Lorenc, S.A., "A Parametric Study of Gas-Particle Flows in Conical Nozzles," AIAA J., Vol. 3, No. 1, January 1965, p. 103.

10. Lorenc, S.A. and Hoffman, J.D., "Correlation of Performance of Conical and Contoured Nozzles for Gas-Particle Flow," AIAA J., Vol. 4, No. 1, January 1966, p. 169.

11. Fein, H.L., "A Theoretical Model for Predicting Aluminum Oxide Particle Size Distributions in Rocket Exhausts," AIAA J., Vol. 4, No. 1, January 1966, p. 92.

12. Crowe, C.T. and Willoughby, P.G., "A Study of Particle Growth in a Rocket Nozzle," AIAA J., Vol. 5, No. 7, July 1967, p. 1300.

13. Sehgal, R., "An Experimental Investigation of a Gas-Particle System," Jet Propulsion Lab. TR 32-238, March 1962.

14. Dobbins, R.A., "Particle Size of Aluminum Oxide Produced by a Small Rocket Motor," Brown Univ., Final Report, Contract JPL 950973, November 1964.

15. Carlson, D.J. and Hoglund, R.F., "Particle Drag and Heat Transfer in Rocket Nozzles," AIAA J., Vol. 2, No. 11, November 1964, p. 1980.

16. Crowe, C.T., "Dynamics of Two-Phase Flow in Rocket Nozzles," Fourth Quarterly Technical Progress Report, 26 May 1962, United Technology Corporation, Contract No. NOW-61-0760-C.

17. Torobin, L.B. and Gauvin, W.H., "Fundamental Aspects of Solids-Gas Flow, Part I: Introductory Concepts and Idealized Sphere Motion in Viscous Regime," Can. J. Chem. Eng., Vol. 37, August 1959, p. 129.

18. Torobin, L.B. and Gauvin, W.H., "Fundamental Aspects of Solids-Gas Flow, Part II: The Sphere Wake in Steady Laminar Fluids," Can. J. Chem. Eng., Vol. 37, October 1959, p. 167.

19. Torobin, L.B. and Gauvin, W.H., "Fundamental Aspects of Solids-Gas Flow, Part III: Accelerated Motion of a Particle in a Fluid," Can. J. Chem. Eng., Vol. 37, December 1959, p. 224.

20. Torobin, L.B. and Gauvin, W.H., "Fundamental Aspects of Solids-Gas Flow, Part IV: The Effects of Particle Rotation, Roughness and Shape," Can. J. Chem. Eng., Vol. 38, October 1960, p. 142.

21. Torobin, L.B. and Gauvin, W.H., "Fundamental Aspects of Solids-Gas Flow, Part V: The Effects of Fluid Turbulence on the Particle Drag Coefficient," Can. J. Chem. Eng., Vol. 38, December 1960, p. 189.

22. Torobin, L.B. and Gauvin, W.H., "Fundamental Aspects of Solids-Gas Flow, Part VI: Multiparticle Behavior in Turbulent Fluids," Can. J. Chem. Eng., Vol. 39, June 1961, p. 113.

23. Sivier, K.R., "Subsonic Sphere Drag Measurements at Intermediate Reynolds Numbers," Ph.D. Thesis, The University of Michigan, 1967.

24. Sivier, K.R. and Henderson, M., "One Component, Magnetic, Support and Balance System for Wind Tunnel Models," NASA CR-1353, 1969.

25. Castleman, R.A., "The Resistance to the Steady Motion of Small Spheres in Fluids," NACA TN 231, February 1928.

26. Schlichting, H., Boundary Layer Theory, 4th ed., McGraw-Hill Book Co., Inc., 1960.

27. Christiansen, E.G. and Barker, D.H., "The Effect of Shape and Density on the Free Settling of Particles at High Reynolds Numbers," A.I.Ch.E.J., Vol. 11, No. 1, January 1965, p. 145.

28. Hamielec, A.E., Hoffman, T.W., and Ross, L.L., "Numerical Solution of the Navier-Stokes Equation for Flow Past Spheres: Part 1. Viscous Flow Around Spheres with and without Radial Mass Effux," A.I. Ch.E.J., Vol. 13, No. 2, March 1967, p. 212.

29. Taneda, S., "Studies of Wake Vortices (III), Experimental Investigation of the Wake Behind a Sphere at Low Reynolds Numbers," Reports of Research Institute for Applied Mechanics (Kyushu Univ., Fuhuoka, Japan), Vol. IV, No. 16, October 1956, p. 99.

30. Schaaf, S.A., "Recent Progress in Rarefied Gasdynamics," ARS J., Vol. 30, No. 5, May 1960, p. 443.

31. Hoerner, S.F., Fluid-Dynamic Drag, (published by the author), 1958.

32. Selberg, B.P. and Nicholls, J.A., "Drag Coefficient of Small Spherical Particles," AIAA J., Vol. 6, No. 3, March 1968, pp. 401-408 (also NASA Contractor Report CR-418, April 1966).

33. Torobin, L.B. and Gauvin, W.H., "The Drag Coefficients of Single Spheres Moving in Steady and Accelerated Motion in a Turbulent Fluid," A.I.Ch.E.J., Vol. 7, No. 4, December 1961, p. 615.

34. Schubauer, G.B. and Dryden, H.L., "Effect of Turbulence on Drag of Flat Plates," NACA TR 546, 1935.

35. Ingebo, R.D., "Drag Coefficients for Droplets and Solid Spheres in Clouds Accelerating in Airstreams," NACA TN 3762, September 1956.

36. Rudinger, G., "Experiments on Shock Relaxation in Particle Suspensions in a Gas and Preliminary Determination of Particle Drag Coefficients," Cornell Aeronautical Laboratory, Project SQUID Tech. Rept. CAL-90-P, July 1963.

37. Crowe, C.T., Nicholls, J.A., and Morrison, R.B., "Drag Coefficients of Inert and Burning Particles Accelerating in Gas Streams," Ninth Symposium (International) on Combustion, Academic Press, 1963, pp. 395-405 (also Ph.D. Thesis, Univ. of Michigan, 1961).

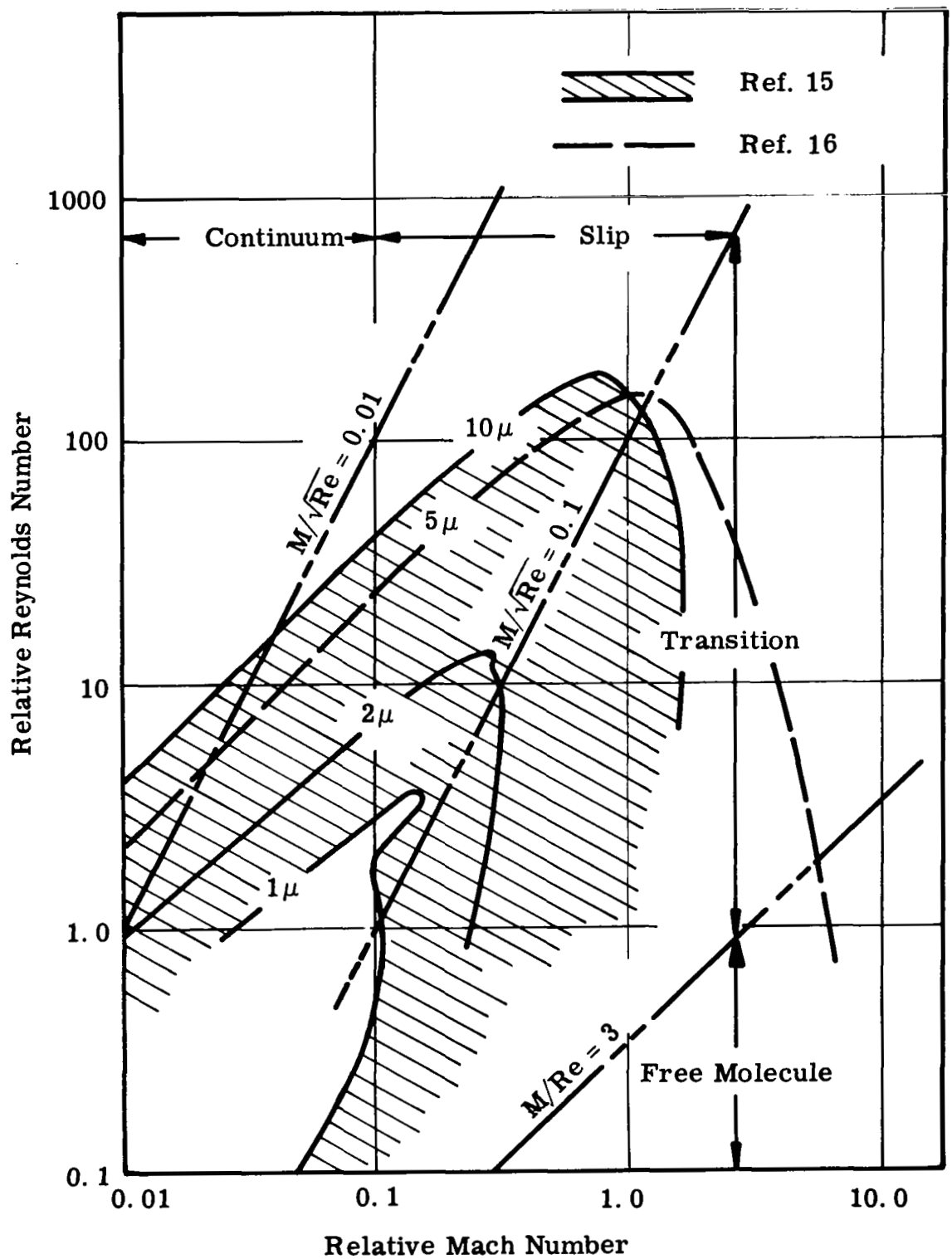

Figure 1. Typical Particle Gas Dynamic Trajectories

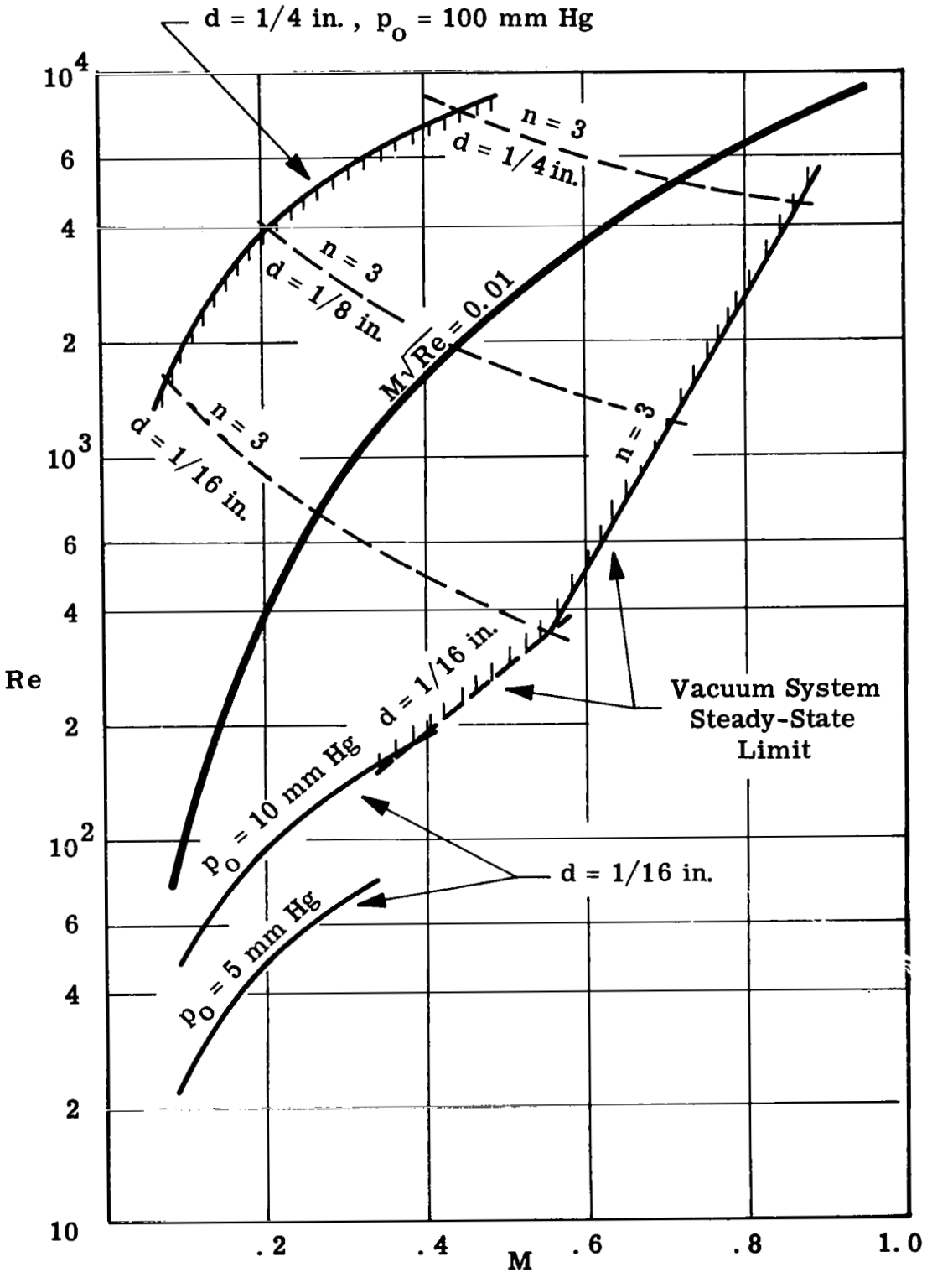

Figure 2. M-Re Performance of Wind Tunnel with Magnetic Balance.

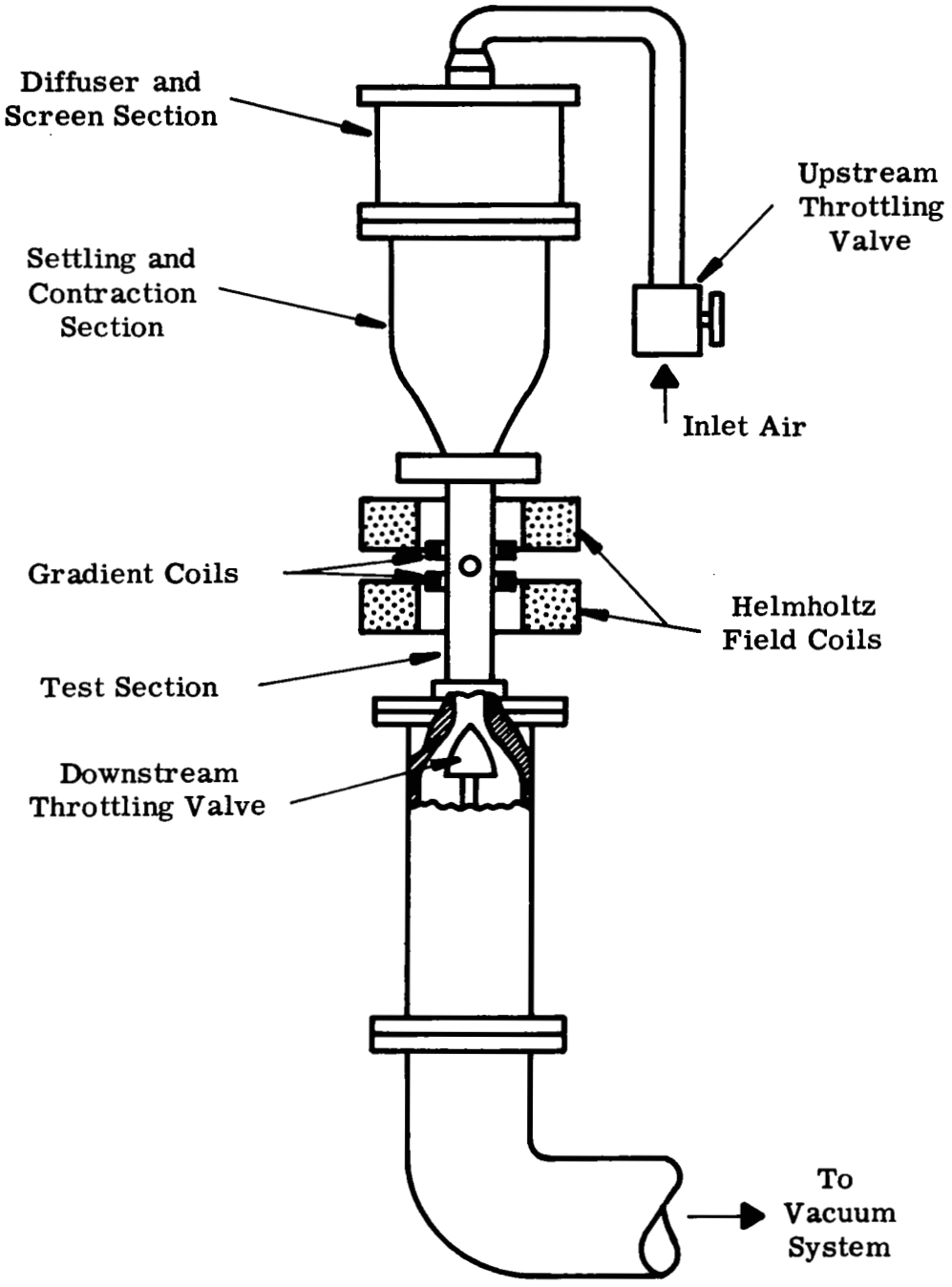

Figure 3. Sketch of Wind Tunnel

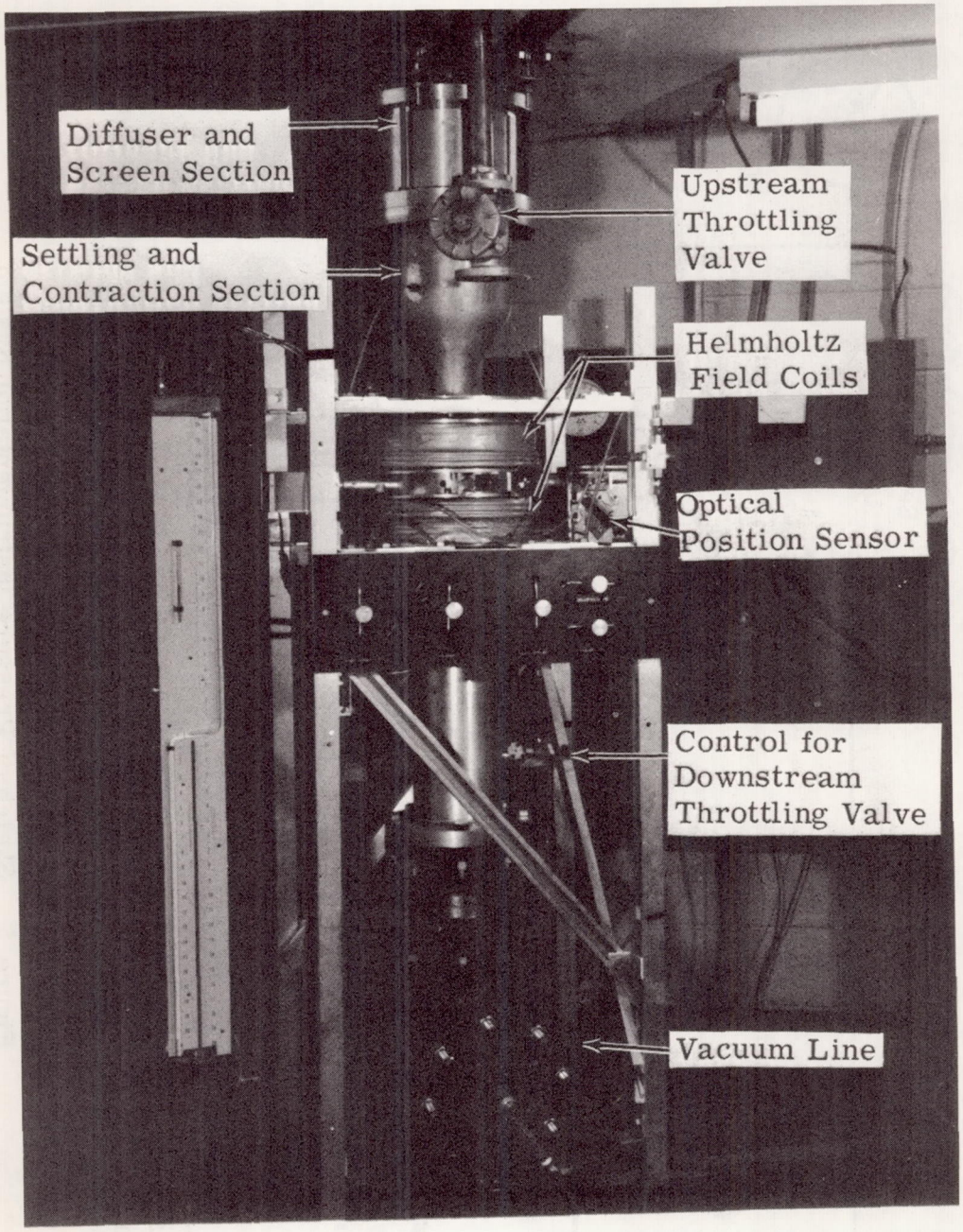

Figure 4. Photograph of Wind Tunnel.

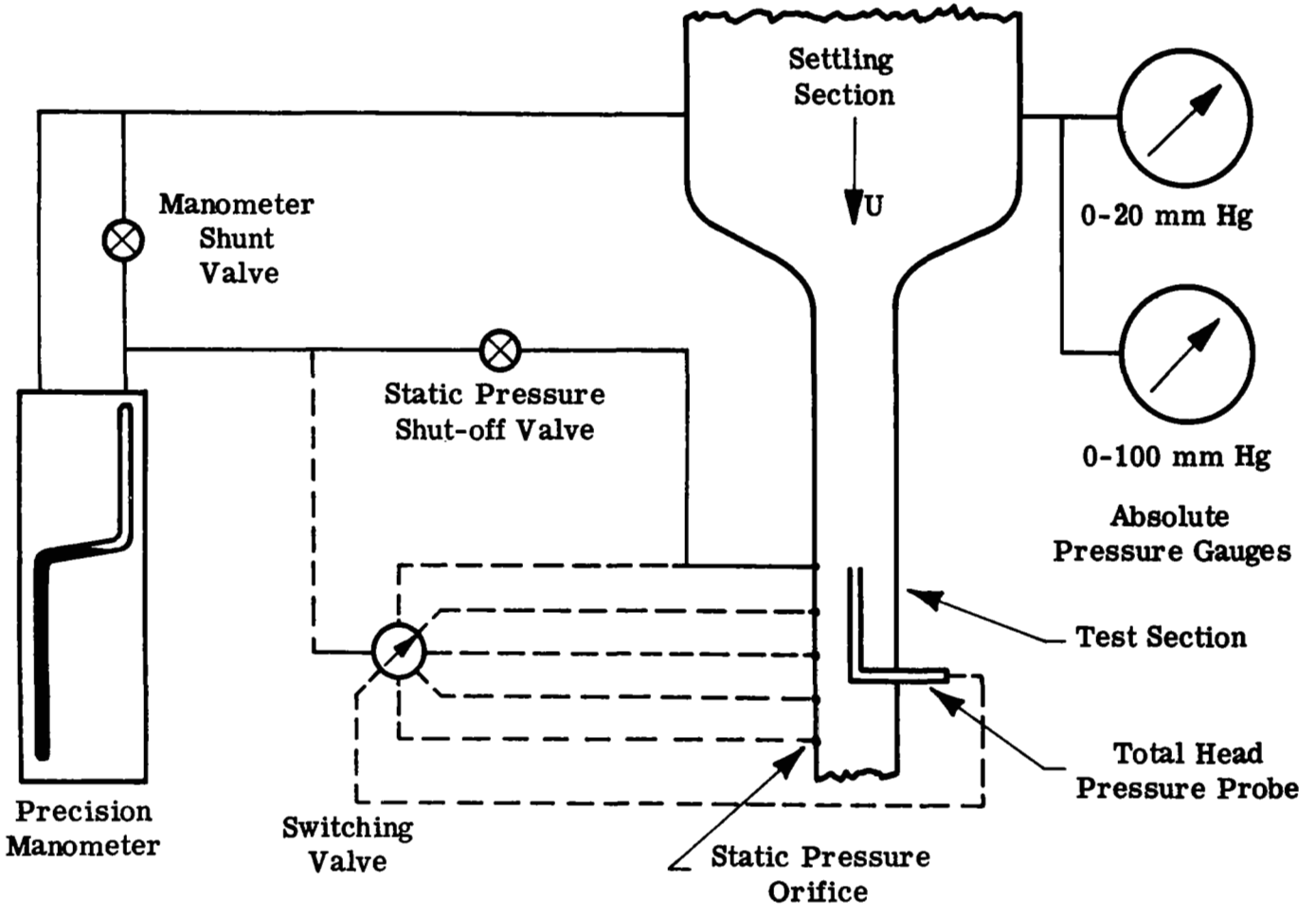

Figure 5. Sketch of Pressure Instrumentation System.

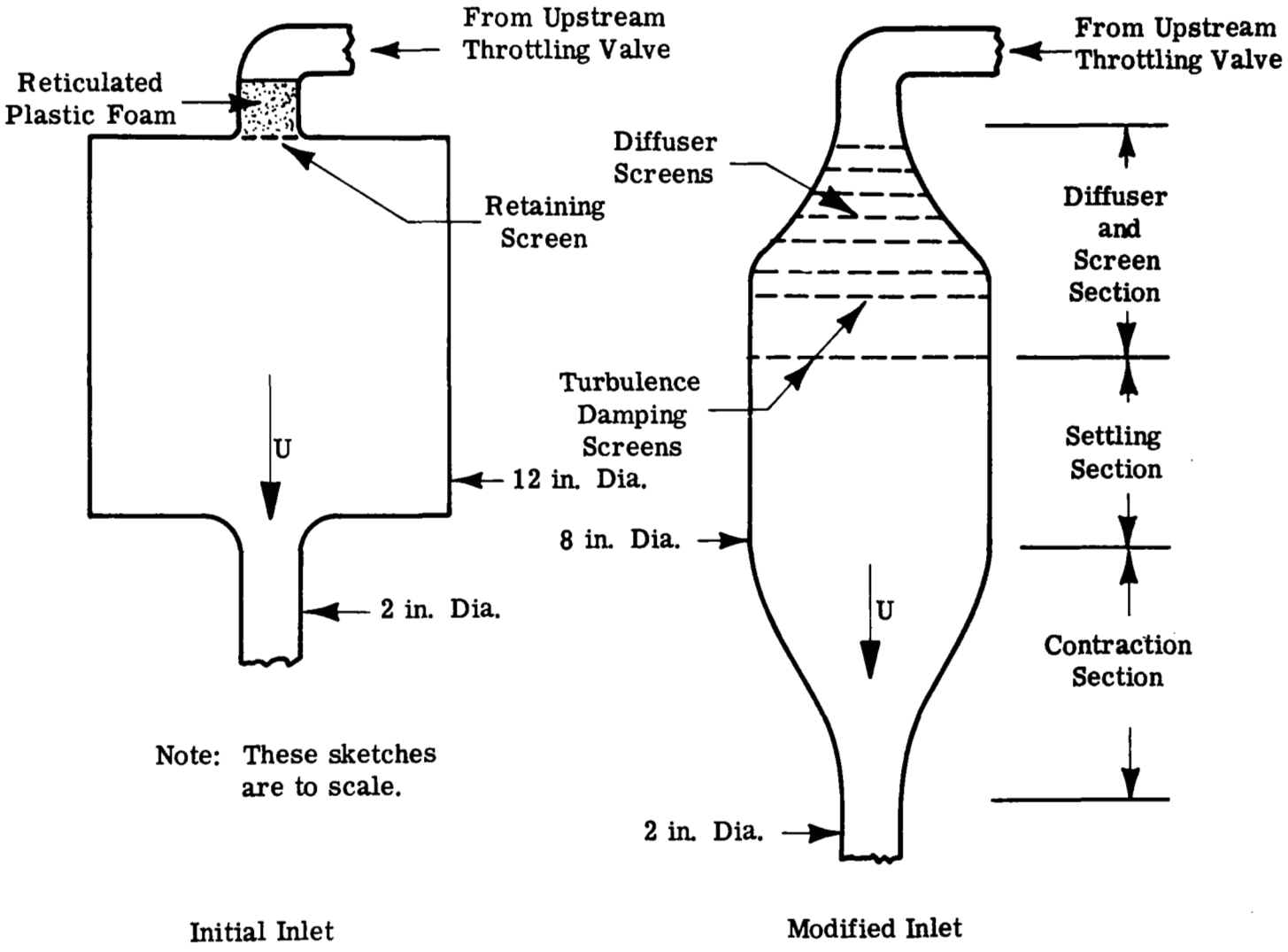

Figure 6. Sketches of Wind Tunnel Inlet Configurations.

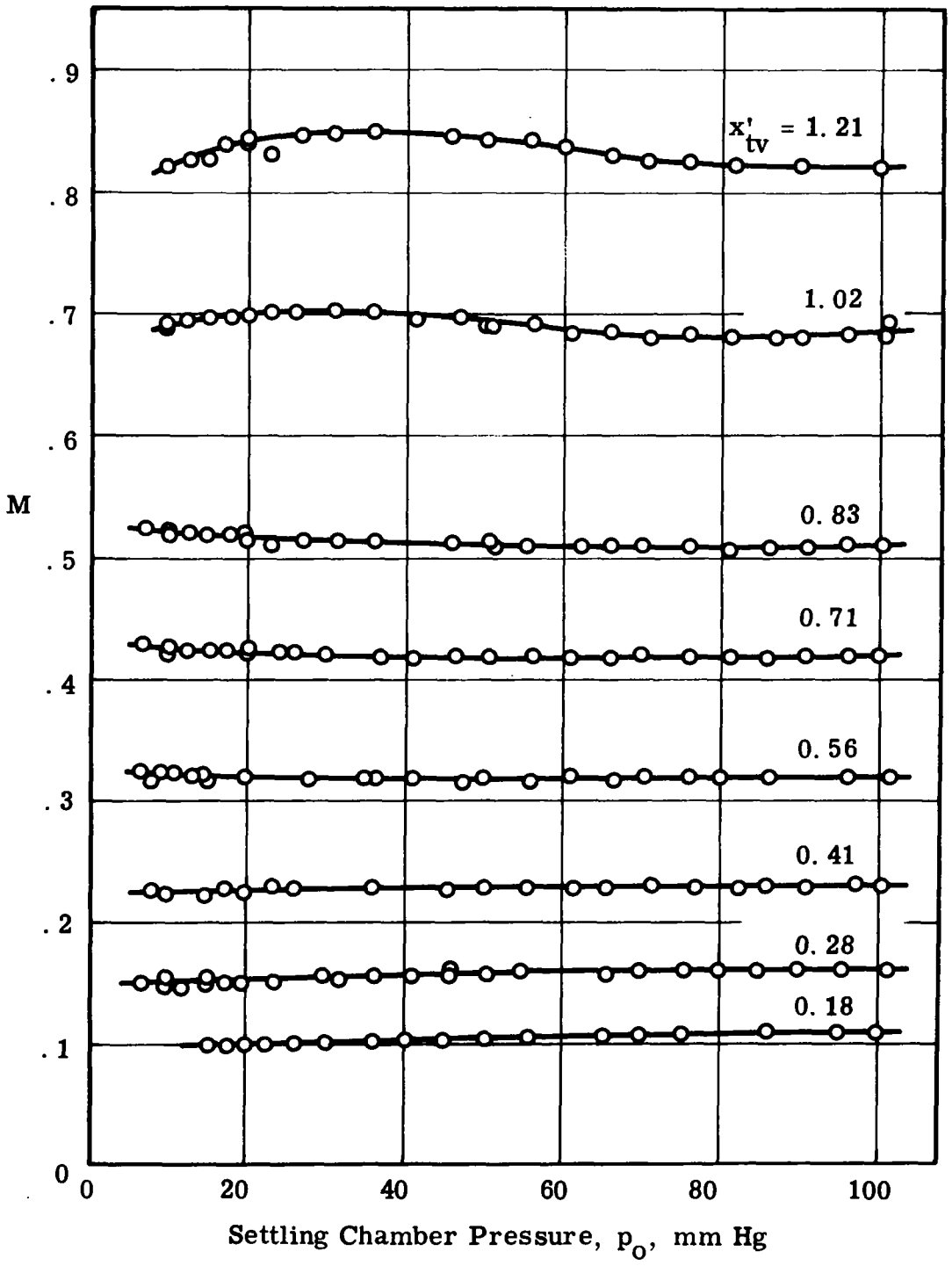

Figure 7. Mach Number Calibration

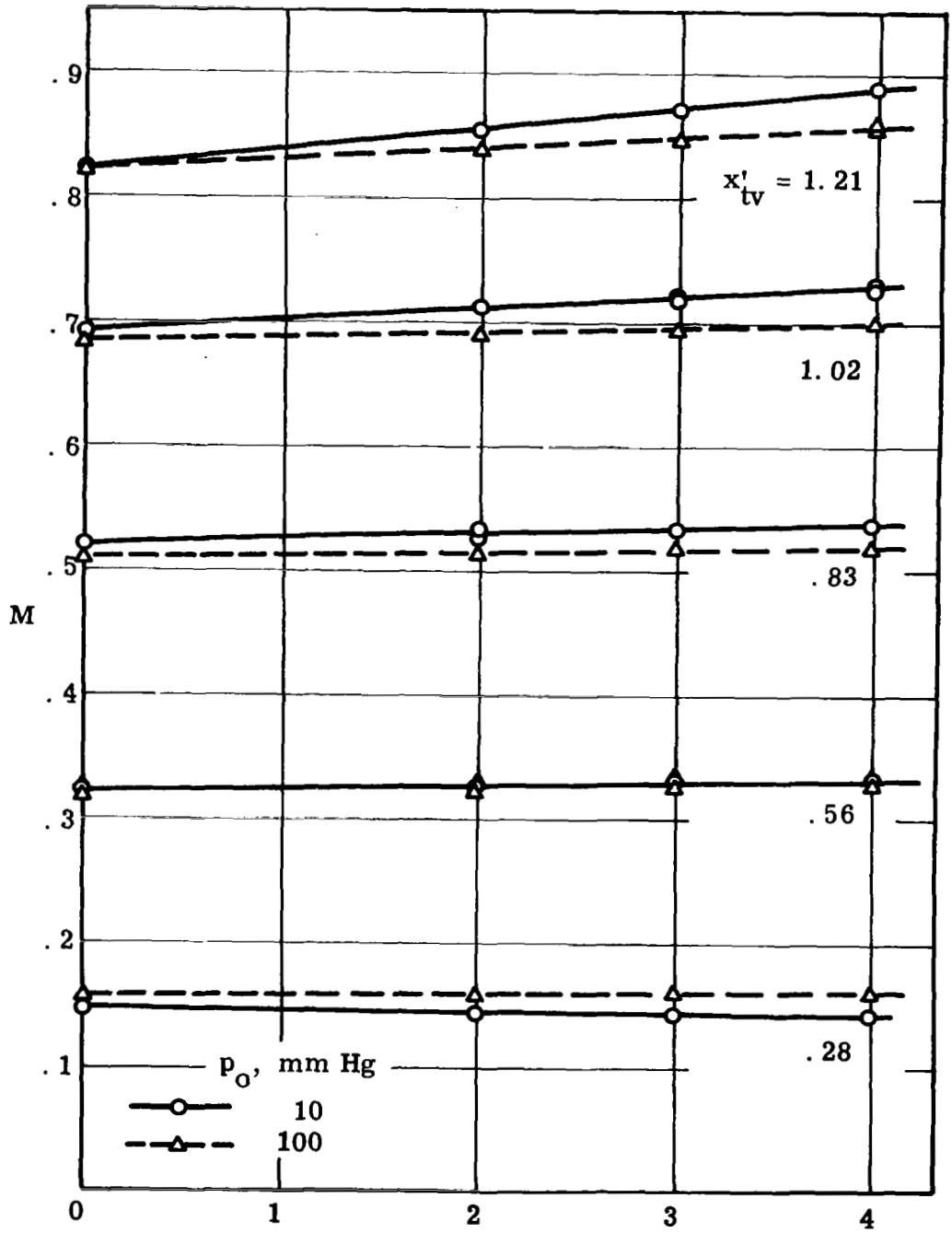

Distance Downstream of Test Section, in.

Figure 8. Axial Mach Number Distributions

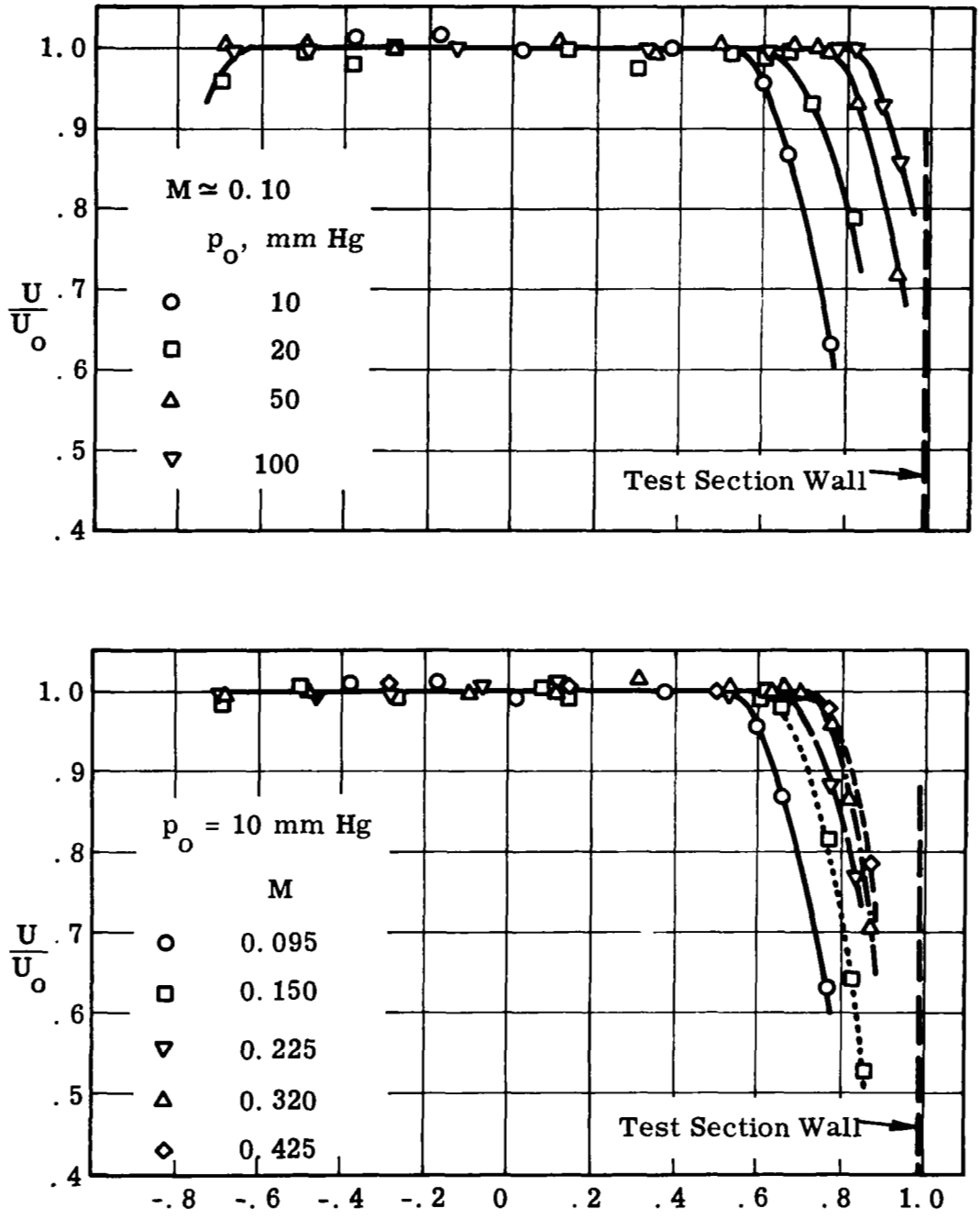

Figure 9. Test Section Velocity Distributions

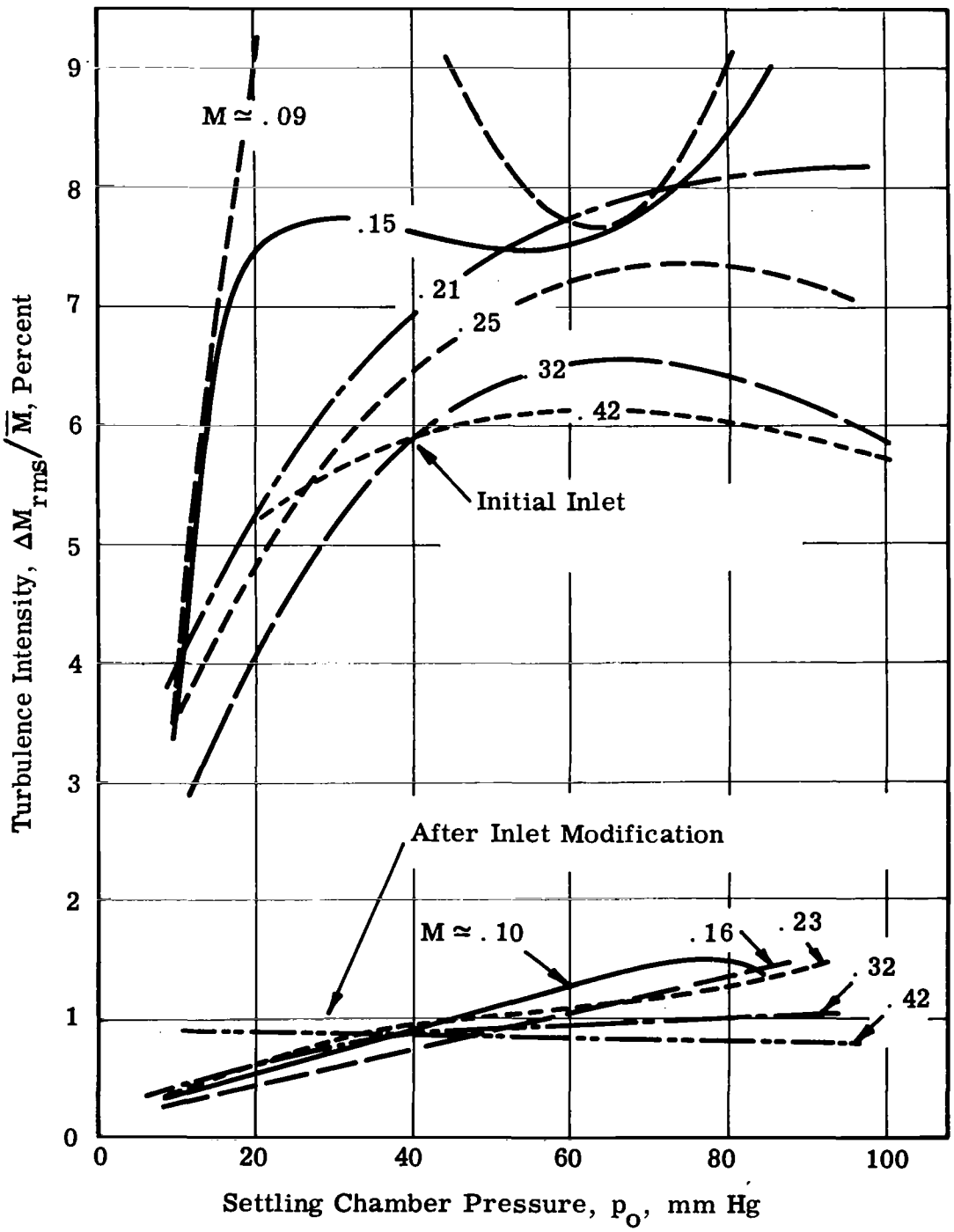

Figure 10. Test Section Turbulence Intensities

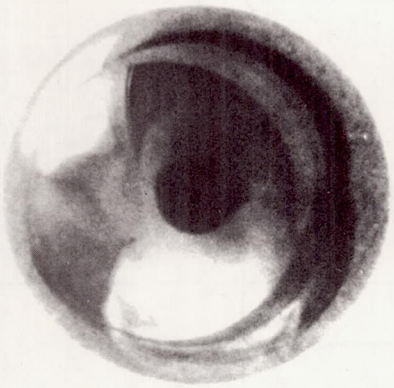

a. Smooth Sphere

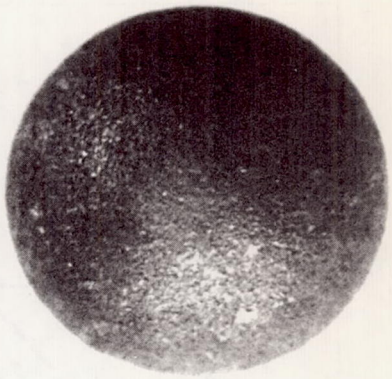

b. Roughened by Tumbling in Grinding Wheel (Initial Effort)

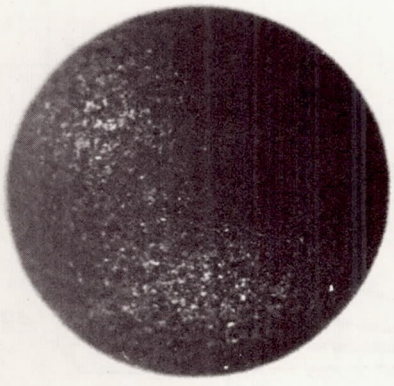

c. Tumbled in Wheel, No. 100 Grit

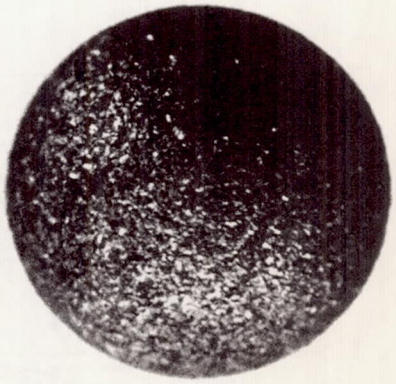

d. Tumbled in Wheel, No. 60 Grit

Note: Spheres have 3/16 in. diameters.

Figure 11. Photographs of Smooth and Roughened Spheres.

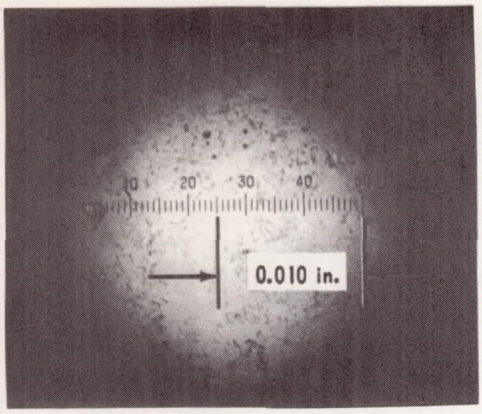

a. Smooth, Grade 5

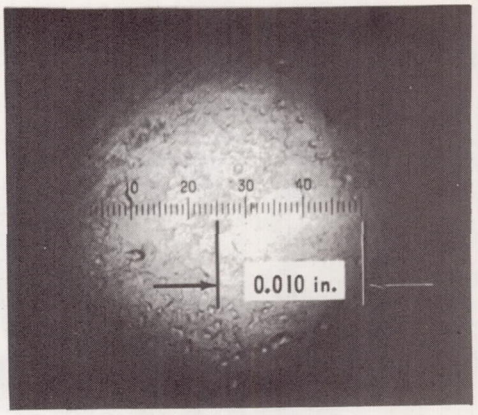

b. Smooth, Grade 25

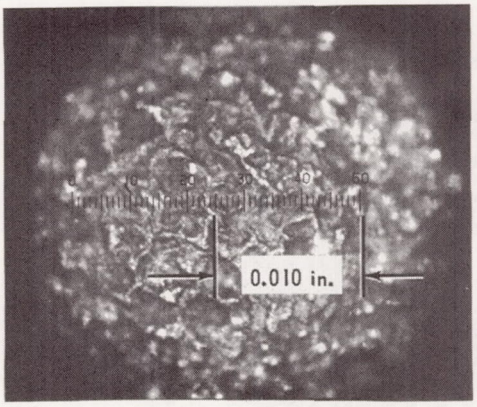

c. Roughened by Tumbling in Grinding Wheel
(Initial Effort)

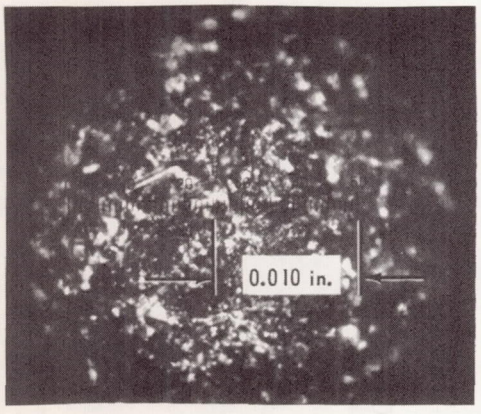

d. Tumbled in Wheel, No. 100 Grit

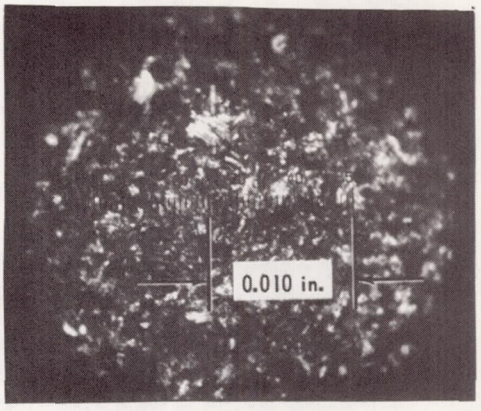

e. Tumbled in Wheel, No. 60 Grit

Figure 12. Photomicrographs of Sphere Surfaces.

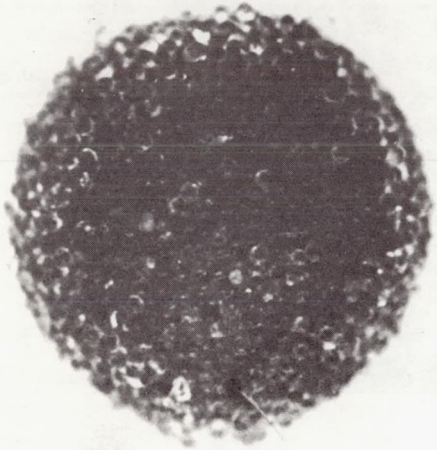

a. 200μ Glass Beads

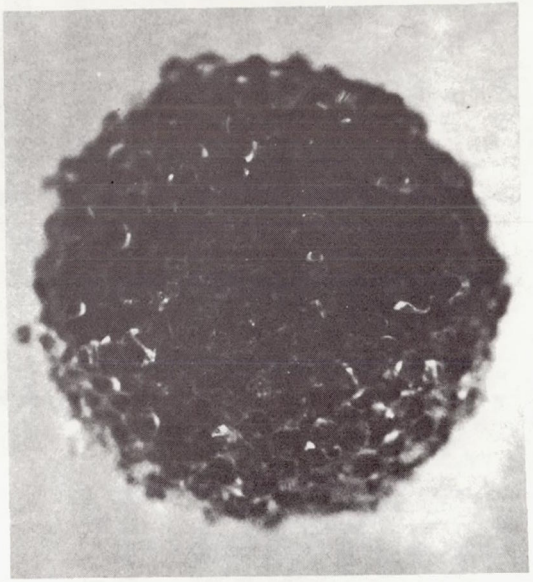

b. 390μ Glass Beads

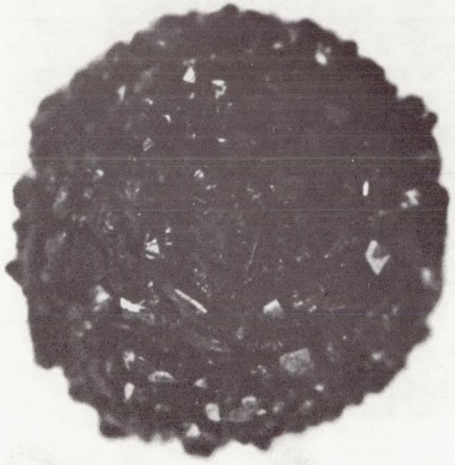

c. No. 60 Grit Abrasive

Note: Core spheres have 3/16 in. diameters.

Figure 13. Photographs of Very Rough Spheres.

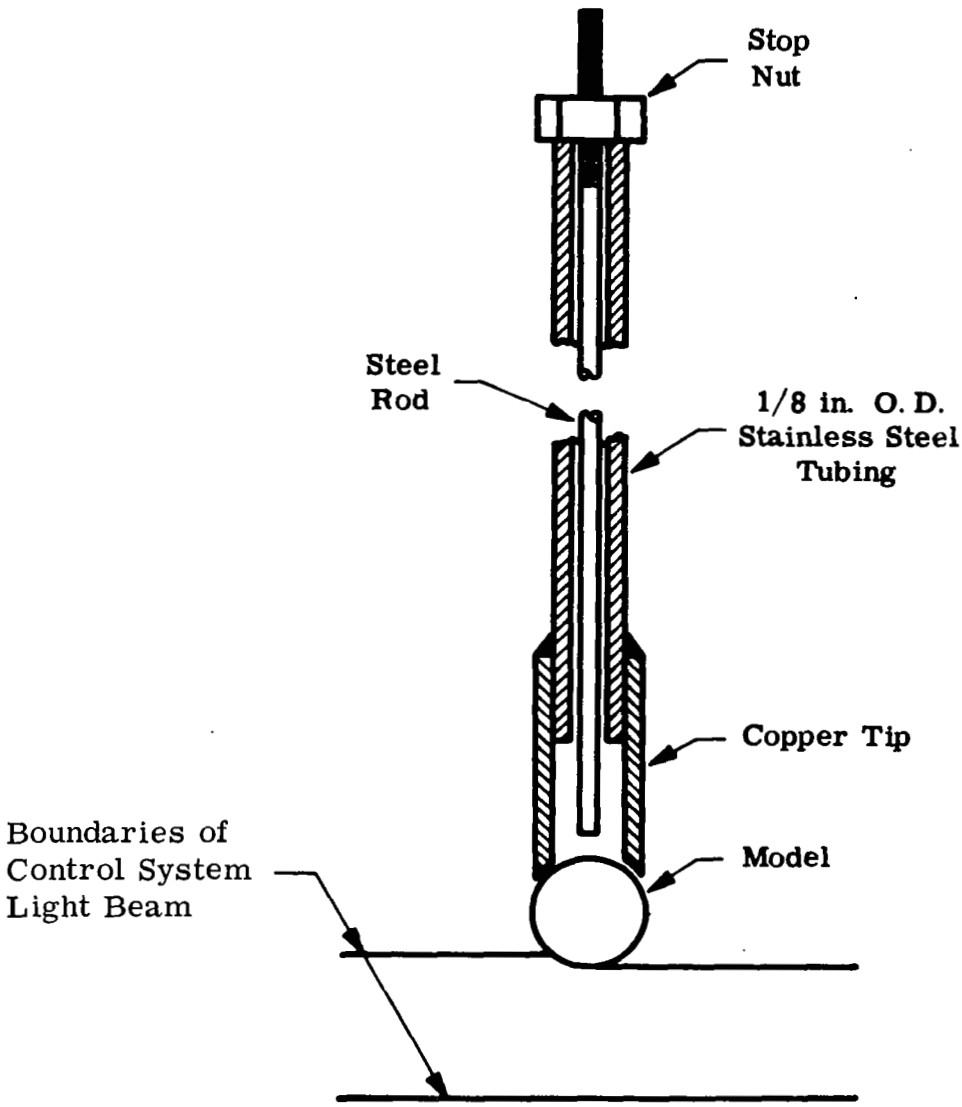

Figure 14. Sketch of Magnetic Model Insertion Probe

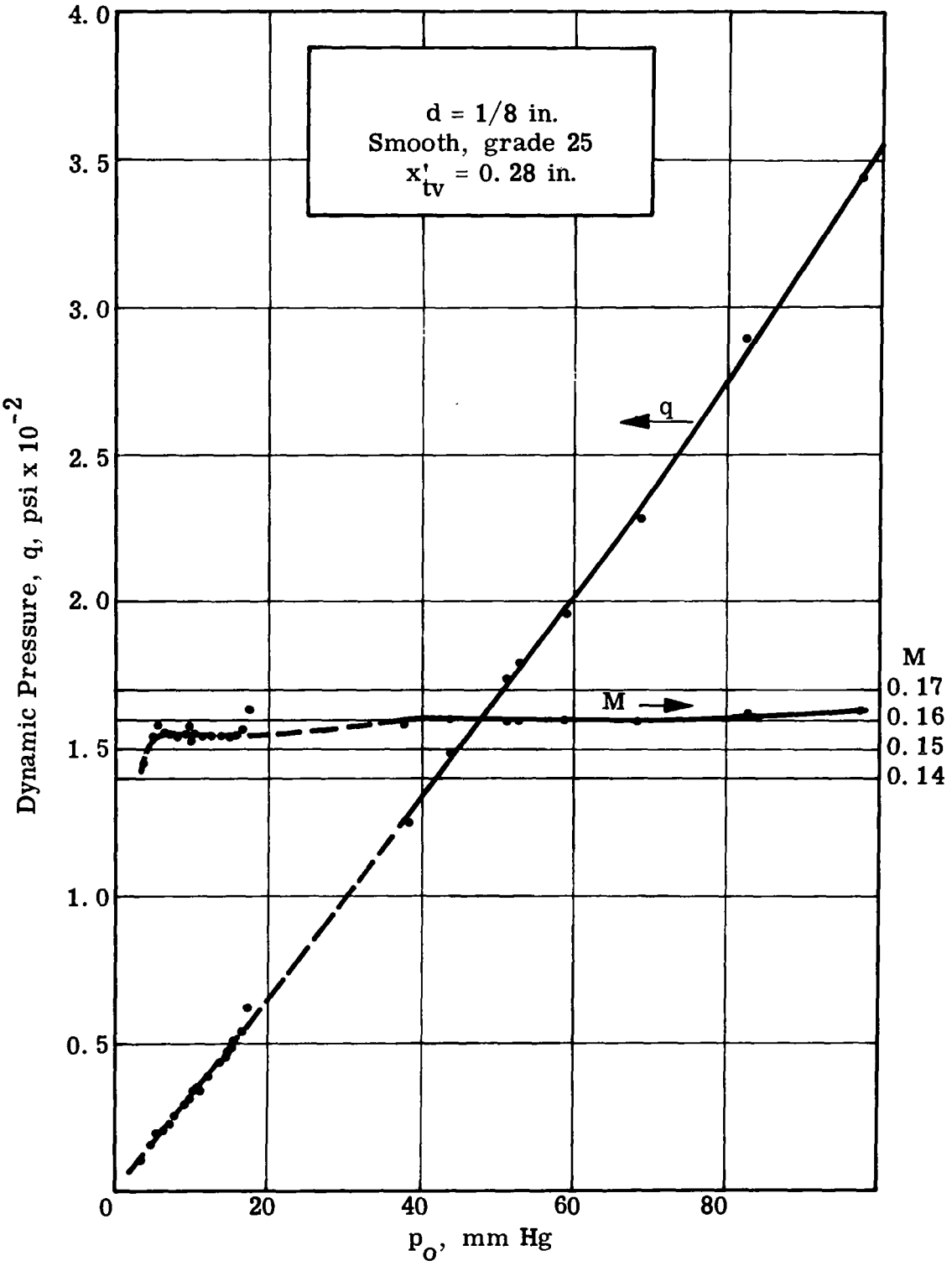

Figure 15(a). Data From Typical Sphere Drag Test.

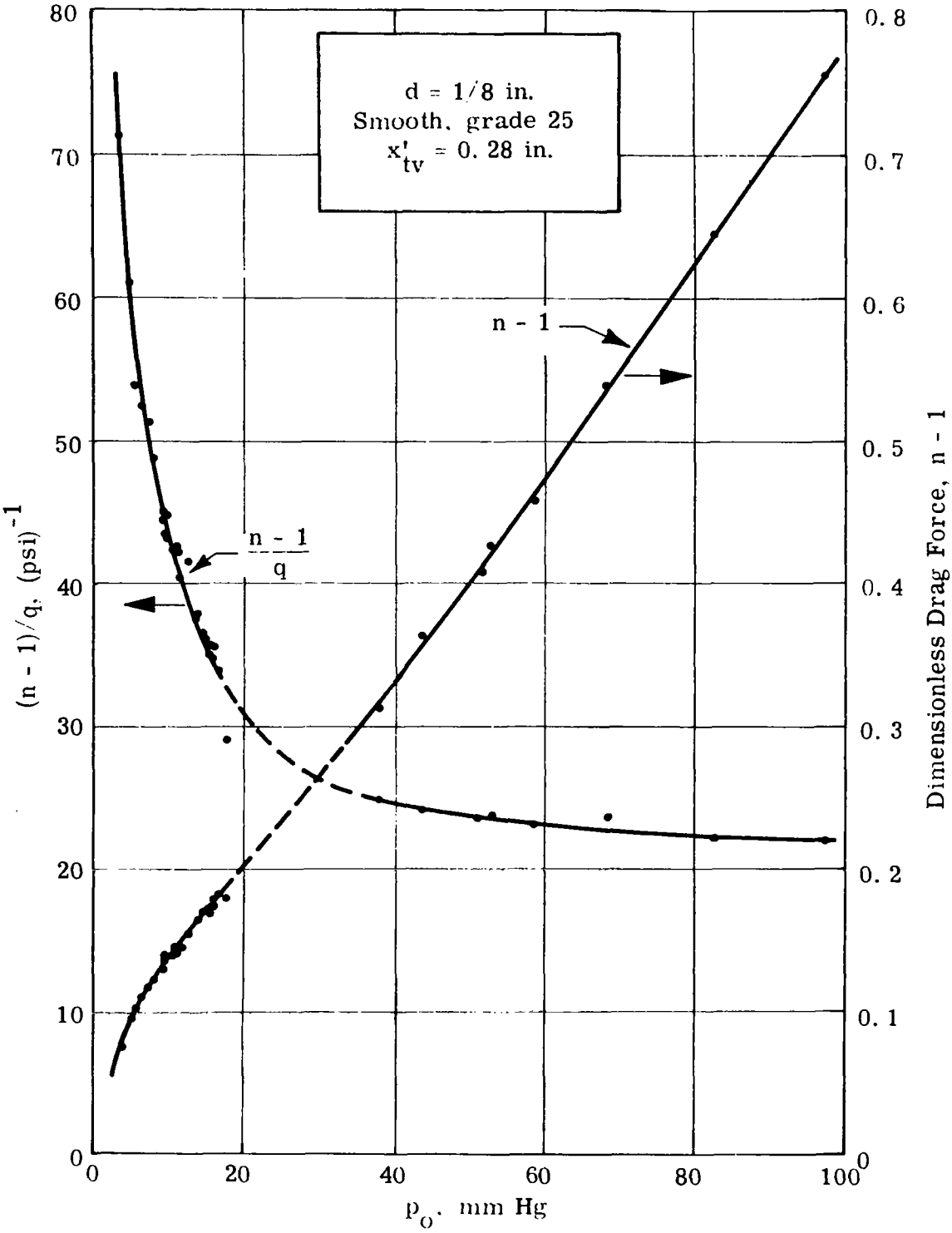

Figure 15(b). Data From Typical Sphere Drag Test.

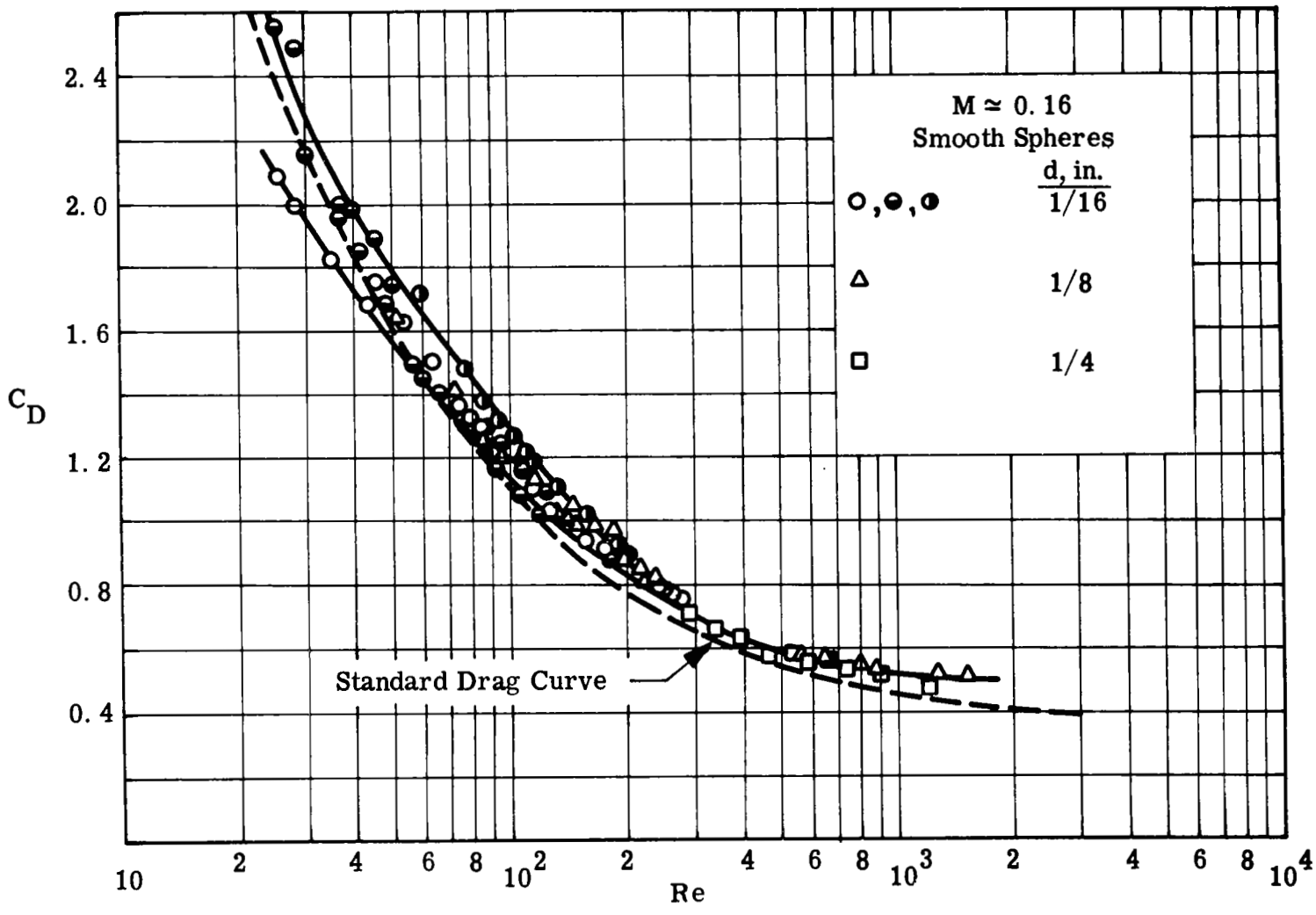

Figure 16. Drag Coefficient of Smooth Spheres; M ≃ 0.16

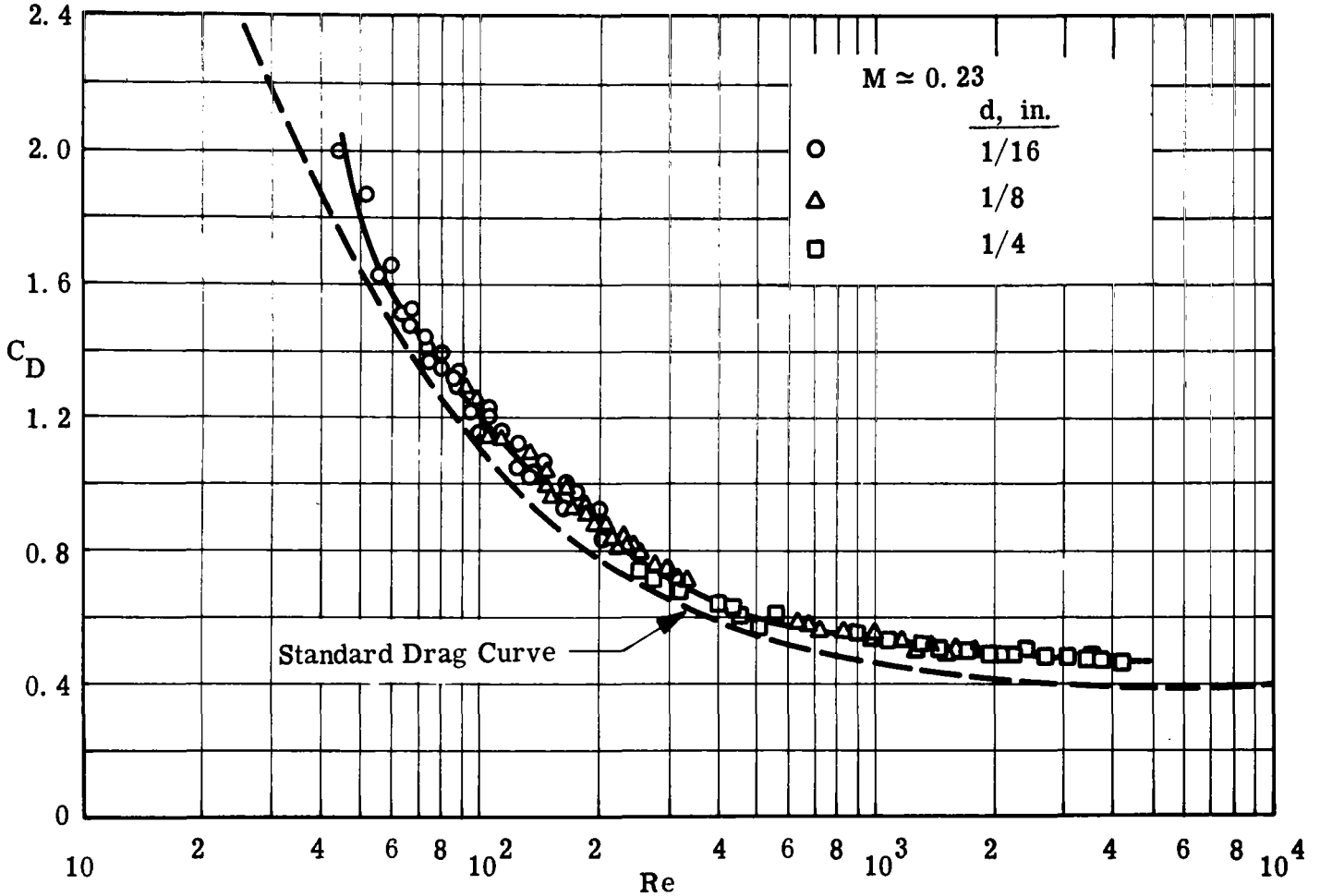

Figure 17. Drag Coefficient of Smooth Spheres; M ≃ 0.23.

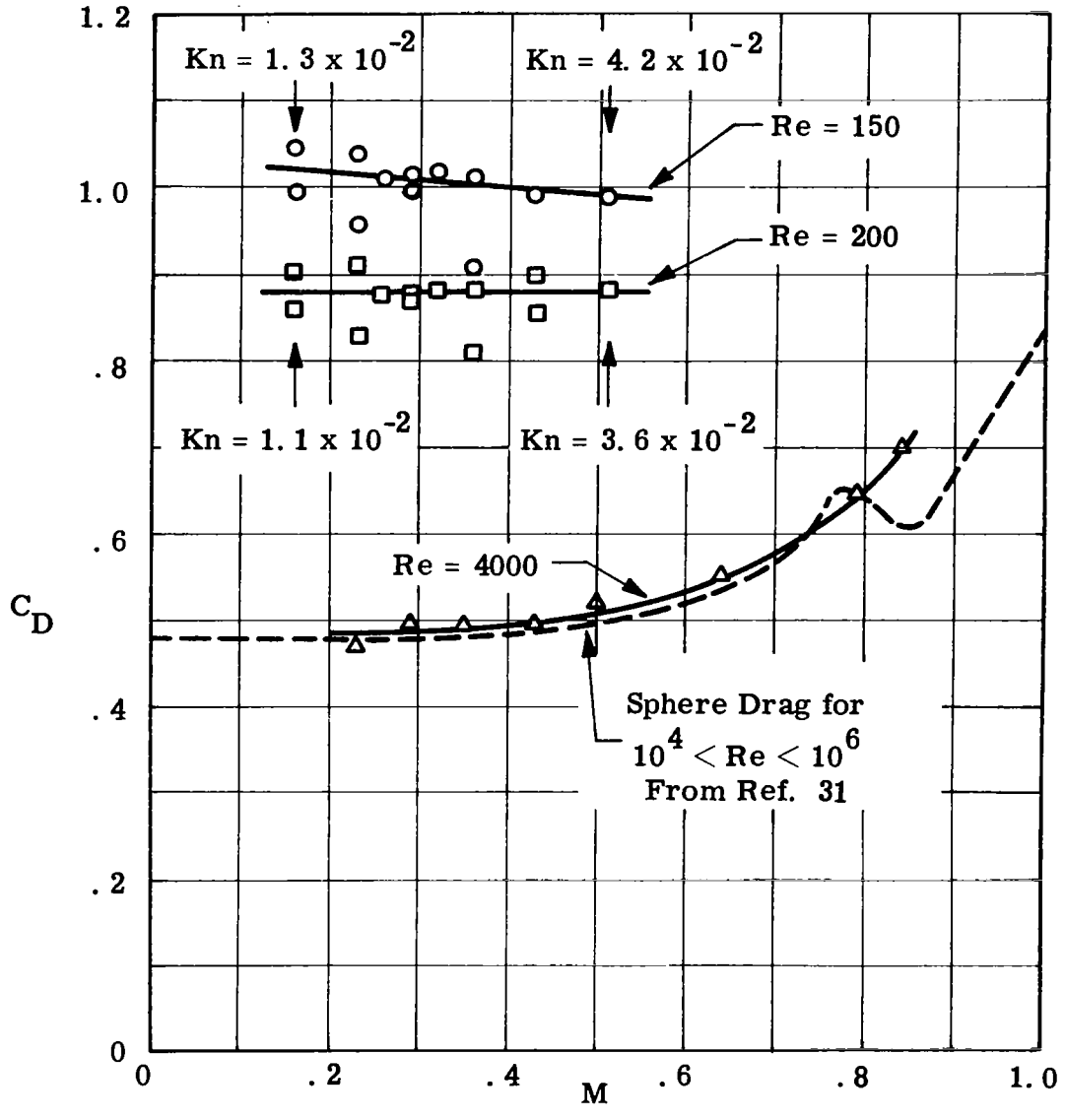

Figure 18. Effect of Mach Number on the Drag of Smooth Spheres

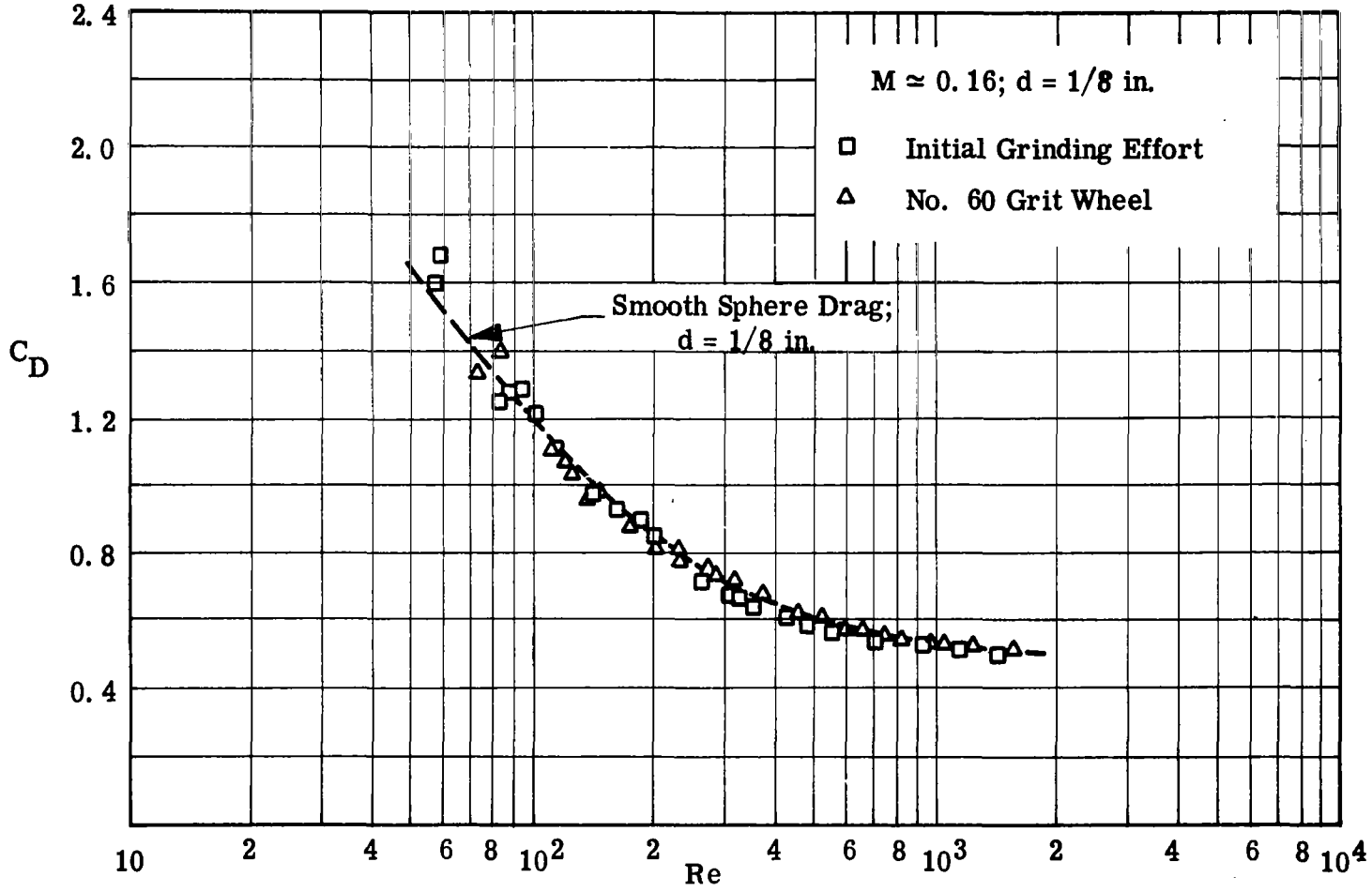

Figure 19. Drag Coefficient of Roughened Spheres.

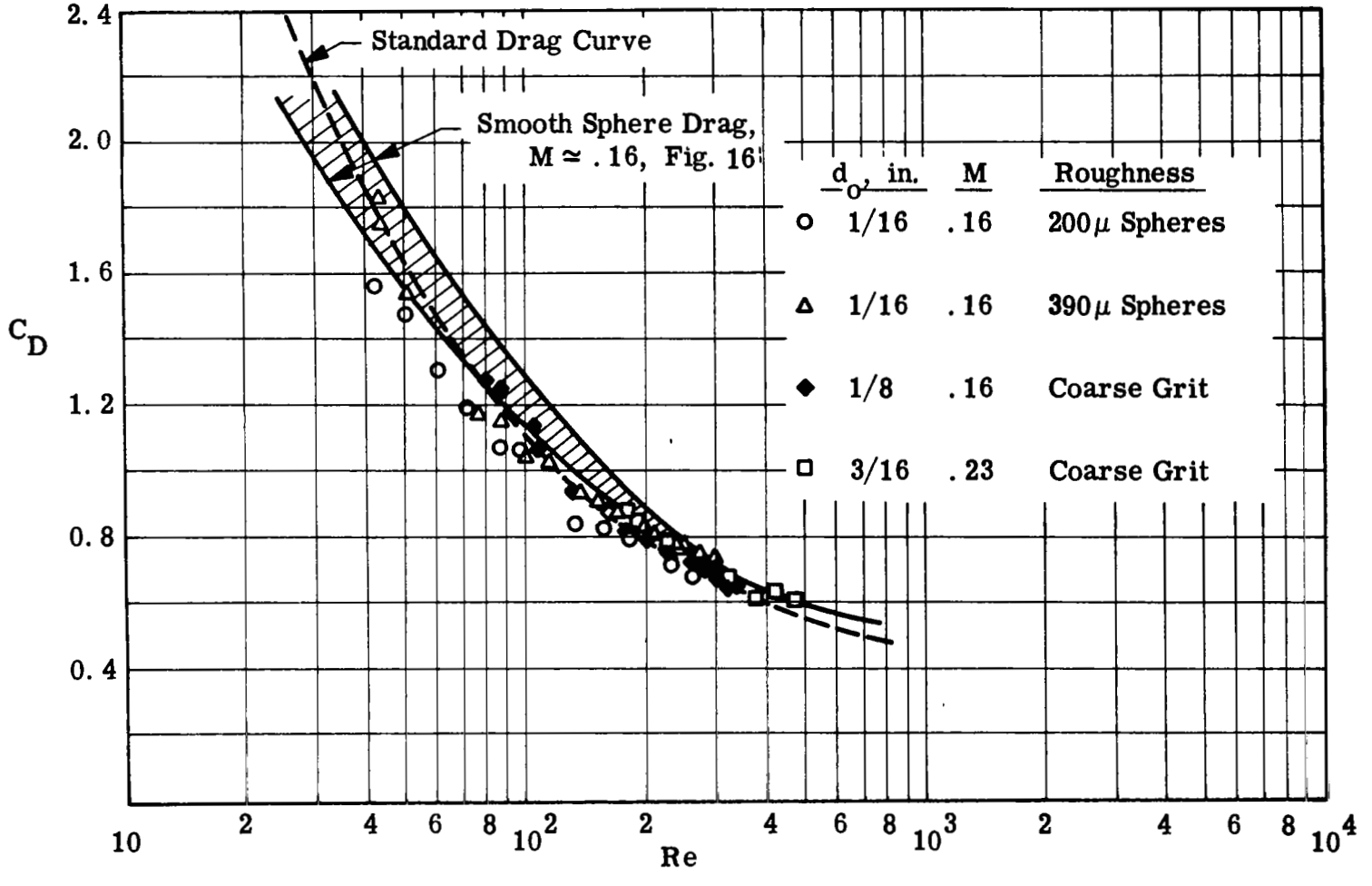

Figure 20. Drag Coefficient of Very Rough Spheres; $40 < Re < 500$

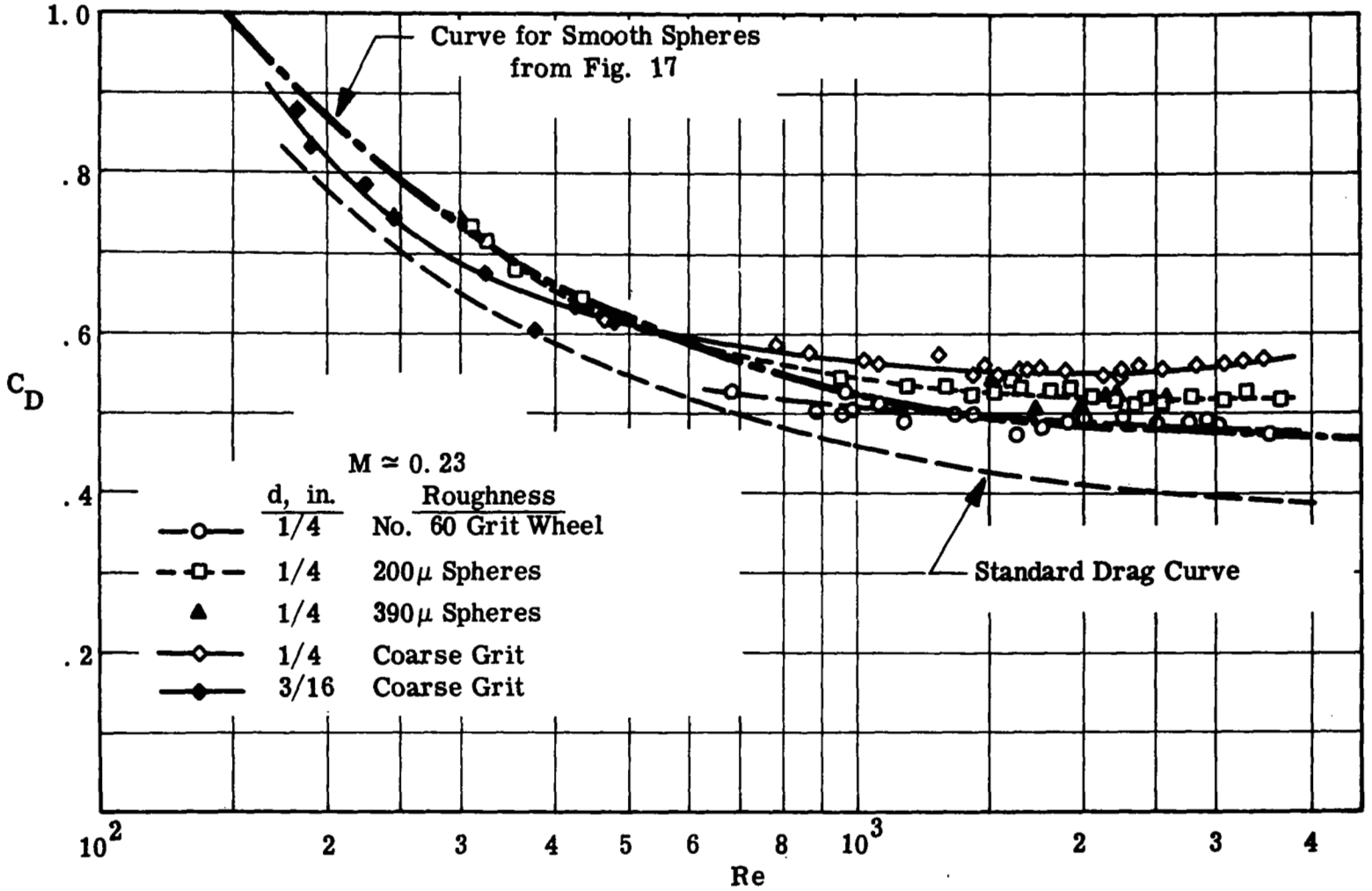

Figure 21. Drag Coefficient of Very Rough Spheres; $200 < Re < 4000$

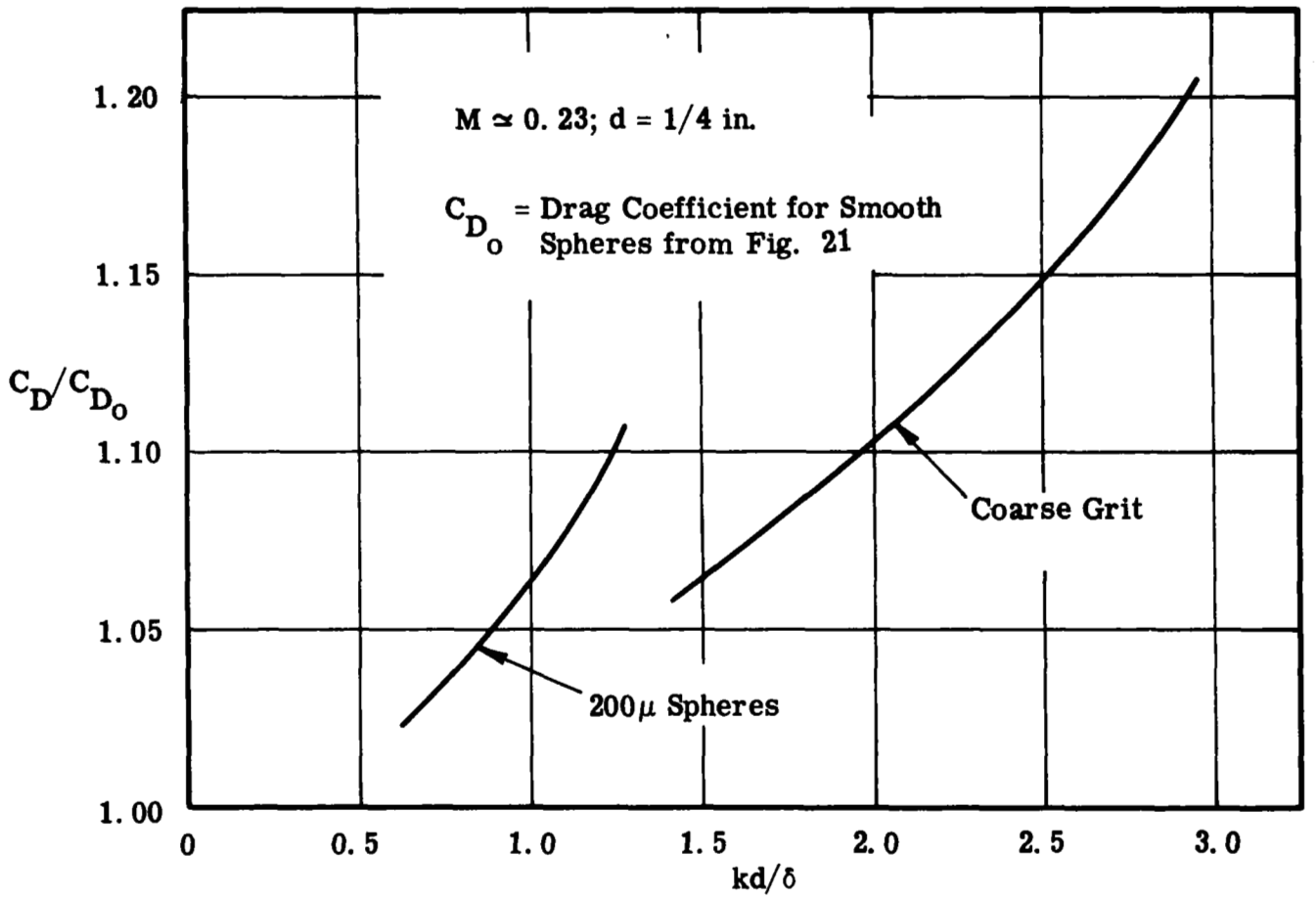

Figure 22. Effect of Roughness on Sphere Drag; $1000 \leq Re \leq 3500$.

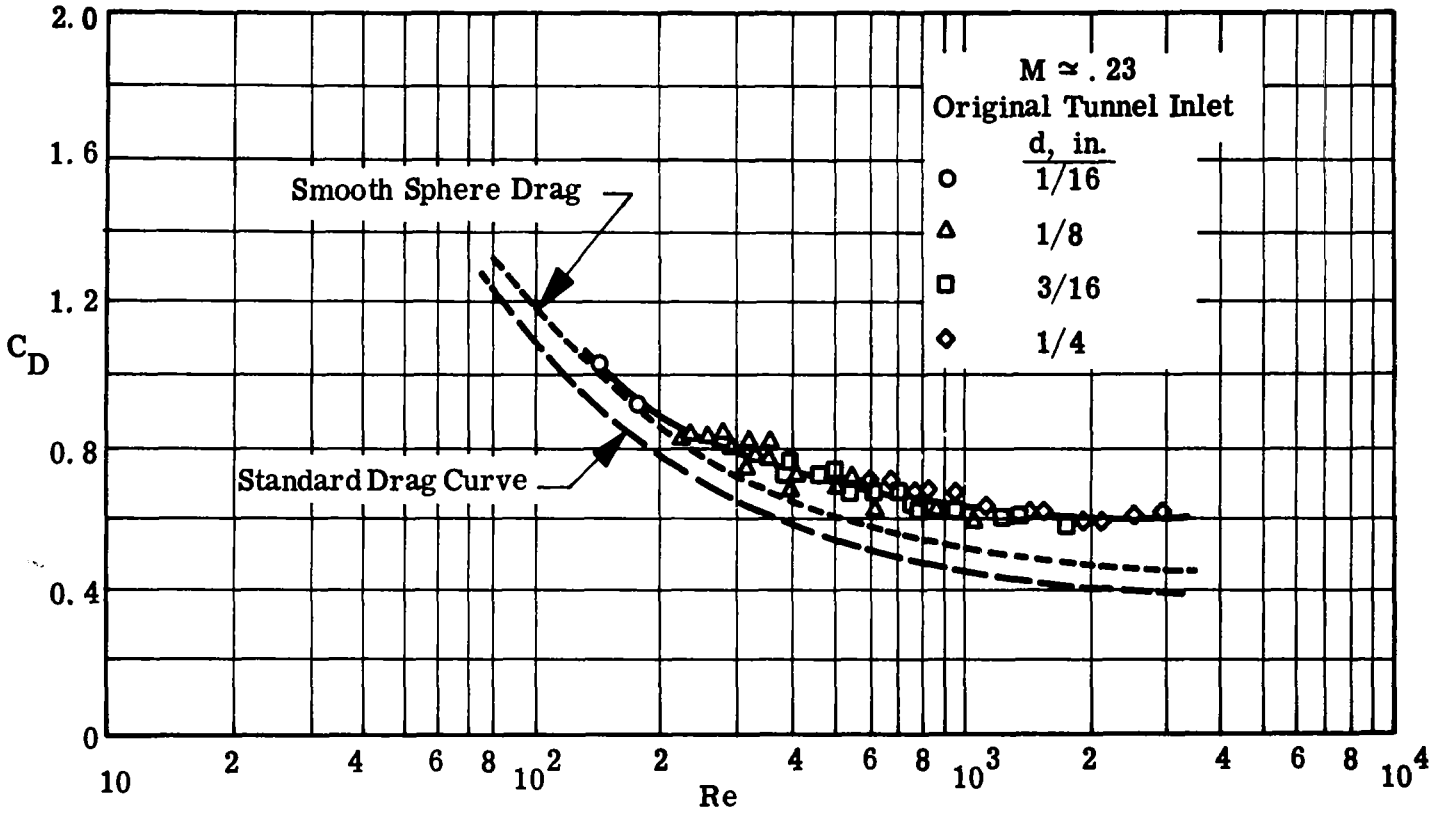

Figure 23. Drag Coefficient of Spheres in Turbulent Flow.

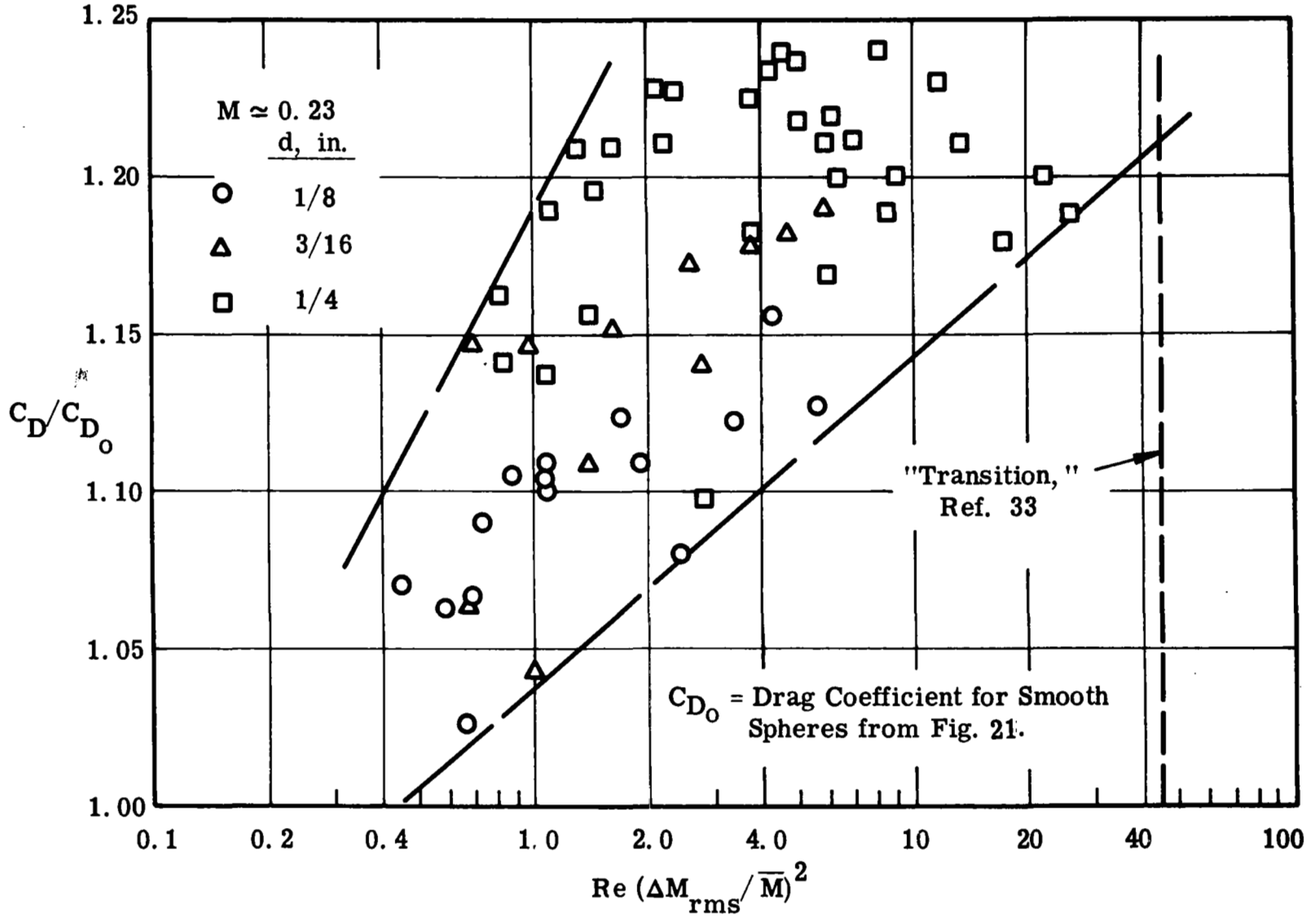

Figure 24. Correlation of Turbulent Drag Rise with Re $(\Delta M_{rms}/\overline{M})^2$.